

# Multifragmentation of a very heavy nuclear system (I): Selection of single-source events<sup>★</sup>

J.D. Frankland<sup>a,1</sup>, Ch.O. Bacri<sup>a</sup>, B. Borderie<sup>a</sup>, M.F. Rivet<sup>a</sup>,  
 M. Squalli<sup>a</sup>, G. Auger<sup>b</sup>, N. Bellaize<sup>c</sup>, F. Bocage<sup>c</sup>,  
 R. Bougault<sup>c</sup>, R. Brou<sup>c</sup>, Ph. Buchet<sup>d</sup>, A. Chbihi<sup>b</sup>, J. Colin<sup>c</sup>,  
 D. Cussol<sup>c</sup>, R. Dayras<sup>d</sup>, A. Demeyer<sup>e</sup>, D. Doré<sup>d</sup>, D. Durand<sup>c</sup>,  
 E. Galichet<sup>a,f</sup>, E. Genouin-Duhamel<sup>c</sup>, E. Gerlic<sup>e</sup>, D. Guinet<sup>e</sup>,  
 Ph. Lantesse<sup>e</sup>, J.L. Laville<sup>b</sup>, J.F. Lecolley<sup>c</sup>, R. Legrain<sup>d</sup>,  
 N. Le Neindre<sup>c</sup>, O. Lopez<sup>c</sup>, M. Louvel<sup>c</sup>, A.M. Maskay<sup>e</sup>,  
 L. Nalpas<sup>d</sup>, A.D. Nguyen<sup>c</sup>, M. Parlog<sup>g</sup>, J. Péter<sup>c</sup>, E. Plagnol<sup>a</sup>,  
 E. Rosato<sup>h</sup>, F. Saint-Laurent<sup>b,2</sup>, S. Salou<sup>b</sup>, J.C. Steckmeyer<sup>c</sup>,  
 M. Stern<sup>e</sup>, G. Tăbăcaru<sup>g</sup>, B. Tamain<sup>c</sup>, O. Tirel<sup>b</sup>,  
 L. Tassan-Got<sup>a</sup>, E. Vient<sup>c</sup>, C. Volant<sup>d</sup>, J.P. Wieleczko<sup>b</sup>

INDRA collaboration

<sup>a</sup>*Institut de Physique Nucléaire, IN2P3-CNRS, F-91406 Orsay Cedex, France.*

<sup>b</sup>*GANIL, CEA et IN2P3-CNRS, B.P. 5027, F-14076 Caen Cedex, France.*

<sup>c</sup>*LPC, IN2P3-CNRS, ISMRA et Université, F-14050 Caen Cedex, France.*

<sup>d</sup>*DAPNIA/SPhN, CEA/Saclay, F-91191 Gif sur Yvette Cedex, France.*

<sup>e</sup>*Institut de Physique Nucléaire, IN2P3-CNRS et Université, F-69622 Villeurbanne Cedex, France.*

<sup>f</sup>*Conservatoire Nationale des Arts et Métiers, 292 rue Saint-Martin, 75141 Paris Cedex 03, France.*

<sup>g</sup>*National Institute for Physics and Nuclear Engineering, RO-76900 Bucharest-Măgurele, Romania*

<sup>h</sup>*Dipartimento di Scienze Fisiche e Sezione INFN, Università di Napoli 'Federico II', I80126 Napoli, Italy.*

PACS: 25.70.-z, 25.70.Pq, 25.60.Pj

---

## Abstract

A sample of 'single-source' events, compatible with the multifragmentation of very heavy fused systems, are isolated among well-measured  $^{155}\text{Gd} + \text{}^{nat}\text{U}$  36 A.MeV

reactions by examining the evolution of the kinematics of fragments with  $Z \geq 5$  as a function of the dissipated energy and loss of memory of the entrance channel. Single-source events are found to be the result of very central collisions. Such central collisions may also lead to multiple fragment emission due to the decay of excited projectile- and target-like nuclei and so-called ‘neck’ emission, and for this reason the isolation of single-source events is very difficult. Event-selection criteria based on centrality of collisions, or on the isotropy of the emitted fragments in each event, are found to be inefficient to separate the two mechanisms, unless they take into account the redistribution of fragments’ kinetic energies into directions perpendicular to the beam axis. The selected events are good candidates to look for bulk effects in the multifragmentation process.

*Key words:* NUCLEAR REACTIONS  $^{nat}\text{U}(^{155}\text{Gd},\text{X})$ ,  $E=36$  A.MeV, central collisions, selection of “fused” systems.

---

## 1 Introduction

The study of the behaviour of nuclear matter under extreme conditions of temperature and pressure, and the possible associated phase transitions, constitutes one of the major axes of research in nuclear physics today. The privileged experimental tools to conduct this study are heavy ion collisions from the sub-relativistic to the ultra-relativistic energy range, coupled with powerful large-acceptance multidetector arrays. With beam energies of a few tens to a few hundreds of MeV per nucleon one hopes to explore the environs of the ‘liquid-gas’ coexistence region, which is predicted to be located at less-than-normal densities and at temperatures below the critical temperature for the phase transition ( $T_C \approx 10\text{--}16\text{MeV}$ ) [1]. In such collisions excited pieces of nuclear matter may be formed with excitation energies comparable to or even greater than nuclear binding energies.

In this bombarding energy range, which has been explored at various experimental facilities around the world over the last decade (e.g. GSI Darmstadt, NSCL Michigan, GANIL Caen), an evolution is observed from evaporative processes, in which light particle emission is the principal mode of decay of hot nuclei with temperatures  $\lesssim 5\text{MeV}$ , to the so-called multifragmentation regime

---

\* Experiment performed at Ganil

<sup>1</sup> Corresponding author.

Permanent address: GANIL, B.P. 5027, F-14076 Caen Cedex, France.

E-mail: frankland@ganil.fr. Tel.: 33 231 454628. Fax: 33 231 454665

<sup>2</sup> present address: DRFC/STEP, CEA/Cadarache, F-13018 Saint-Paul-lez-Durance Cedex, France.

where large numbers of nuclei with a wide variety of masses are observed in the exit channel of individual collisions [2,3]. The goal of multifragmentation studies is to link this experimental observation to the properties of the nuclear matter phase diagram, which entails disentangling dynamical effects linked to the collision phase from decay products of thermodynamically equilibrated excited nuclear systems.

For heavy-ion collisions between 20 and 100 A.MeV incident energy, the binary character of almost all reactions has been established experimentally [4–9] either by the identification of surviving projectile-like and target-like fragments (PLF and TLF, respectively) or through the observation of reaction products’ characteristics compatible with their origin in the statistical decay of two principal primary excited nuclei, the quasi-projectile (QP) and quasi-target (QT). It was first thought that such binary reaction mechanisms were essentially a continuation of the deep-inelastic collisions well-known at lower energies [10,11], accompanied by increasingly important “preequilibrium” or “prompt” emissions due to the opening of the phase-space for nucleon-nucleon collisions. However, increasingly exclusive experiments with  $4\pi$  detector arrays have shown that an important fraction of the detected particles and heavier fragments originate from the rapidity region between the projectile and target [12], and that this contribution is difficult to distinguish from that which may be ascribed to the decay of fully equilibrated QP and QT [13,14]. They may, depending on the species considered, the beam energy, system size and impact parameter, find their origin in e.g. prompt emissions from the overlap (participant) zone between the two colliding nuclei [15,16], decay of highly-deformed QP/QT [17,18], or the formation and rupture of a necklike structure between projectile and target [19–22].

Faced with such a highly complex situation for most of the collisions, the so-called “single-source” events observed for a small ( $\sim 1\%$ ) part of the cross-section for collisions of very heavy ions around the Fermi energy [23–25] are of great interest. In these events, all of the emitted fragments and particles, apart from a small preequilibrium component of light particles, seem to originate in the multifragmentation of a single nuclear system containing almost all of the available mass and energy of the entrance channel, which simplifies enormously the analysis. Such events provide a unique opportunity to study the decay of well-defined and very heavy pieces of excited nuclear matter, for which one expects that bulk effects, if present (for example the mechanical instability associated with spinodal decomposition [26–28]), should play a dominant role. Semi-classical transport calculations [29,30] predict these reactions to occur for central collisions of heavy nuclei ( $b < 0.3b_{max}$ ). The initial system formed should therefore suffer large amounts of compression and heating, and may subsequently expand into the low-density coexistence region.

The method by which a certain set of data is selected depends on the exper-

imental conditions, detector systems and the reaction studied. In the present work we present in detail the procedure by which single-source events have been brought to light and isolated for  $^{155}\text{Gd} + ^{\text{nat}}\text{U}$  36 A.MeV reactions studied with INDRA. The method used (based on the angle  $\theta_{\text{flow}}$  signifying the polar deviation from the beam direction of the events' principal axis ) has already been published elsewhere [23,25], but no comparison has been made before between this method and other procedures which are far more commonly used to sort experimental data in the specific context of single-source event selection. This is the goal of this paper. In the accompanying paper [31] we will use these data in order to probe the role of bulk effects in the multi-fragmentation of such heavy systems.

The experimental set-up, including the detector array specifications and operating conditions during the experiment, is presented in Sec.2. The first step towards an unbiased global reconstruction of the recorded reactions is to ensure that a very large proportion of the emitted products have been measured event by event : this is achieved by an initial selection of ‘complete events’ (Sec.3.1). In order to introduce the comparison between different selection methods, the most commonly used global variables are presented in Sec.3.2 and 3.3. Then the evolution of the reactions from binary collisions to single-source events is described in Sec.4 by classifying them according to  $\theta_{\text{flow}}$ . Finally in Sec.5 we show that the most commonly-used selection methods are generally less efficient for isolating single-source events by comparison with the  $\theta_{\text{flow}}$  selection.

## 2 Experimental details

The  $^{155}\text{Gd} + ^{\text{nat}}\text{U}$  system was studied with the  $4\pi$  multidetector INDRA, operating at the GANIL accelerator. INDRA, which was described in detail in [32,33], can be viewed as an ensemble of 336 telescopes covering  $\sim 90\%$  of the  $4\pi$  solid angle. The detection cells are distributed amongst 17 rings centred on the beam axis. Low energy identification thresholds and large energy ranges were obtained through the design of three-layer telescopes, composed of an axial-field ionization chamber operated at 30 mbars of  $\text{C}_3\text{F}_8$ , a  $300\ \mu\text{m}$  silicon detector and a CsI(Tl) scintillator, thick enough to stop all emitted particles, coupled to a phototube. Such a telescope can detect and identify from protons between 1 and 200 MeV to uranium ions of 4 GeV. Past  $45^\circ$ , where fast projectile-like fragments are no longer expected, the telescopes comprise only two stages, the ionization chamber operated at 20 mbars and the scintillator. Finally the very forward angles ( $2\text{--}3^\circ$ ) are occupied by Ne102–Ne115 phoswiches. Charge resolution of one unit was obtained up to  $Z=64$  for the fragments identified through the  $\Delta E - E$  method in the Si–CsI couple, and up to  $Z=20$  when the  $\Delta E$  signal is furnished by the ionization chamber (above this limit imposed by the energy resolution of the ionization chambers, extrapola-

tion of the identification to heavier fragments is assured by calculations based on energy-loss tables, with a resolution of a few charge units).

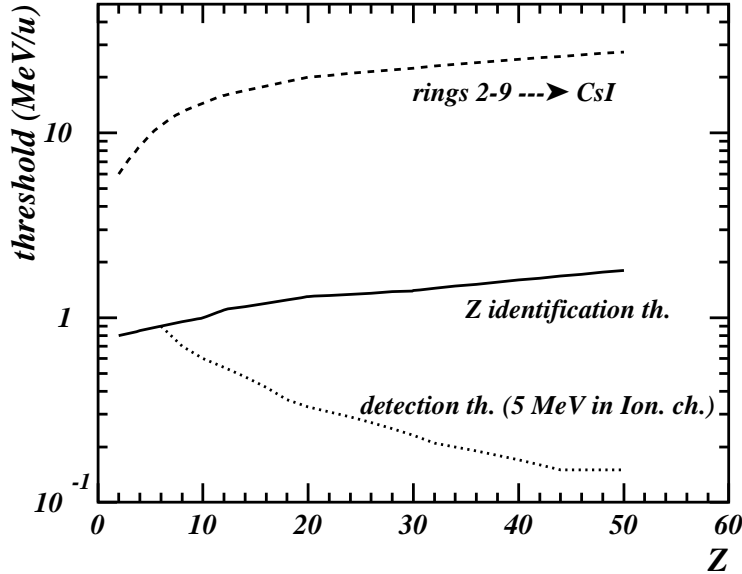


Fig. 1. Energy thresholds of the 3-member INDR A modules. full line: charge identification thresholds; dashed line: minimum energy to reach the CsI; dotted line: detection threshold (ions depositing 5 MeV in the ionization chamber, but not identified).

Identification thresholds increase from  $\sim 0.7$  A.MeV for  $Z=3$  to  $\sim 1.7$  A.MeV for  $Z=50$  (Fig.1). Slow heavy ions at around or just below the threshold energy, stopping in the detector directly behind the ionization chamber, are partially identified i.e. are assigned a minimum atomic number. In our analysis such particles are only included to permit the global characterisation of the least violent collisions, when fission fragments of the target nucleus (see Fig. 8(a) and accompanying discussion in the text) are present. Energy calibration of all detectors ensured an accuracy of within 5%. Great attention was paid to pulse-height defect calibration of the *Si*-300 $\mu$ m detectors for fragments  $Z \geq 15$  [34]. For Rings 2–9 residual energy deposited in *CsI* scintillators were derived from energy losses in the (preceding) silicon detectors. Energy calibrations of *CsI* scintillators were only performed for Rings 10–17 ( $45 \leq \theta_{lab} \leq 176^\circ$ ) and were recently improved with a better description of quenching which was previously over-estimated because  $\delta$ -electrons were neglected [35]: measured kinetic energies of fragments with  $Z \approx 15$ –35 detected beyond  $45^\circ$  for the  $^{155}\text{Gd} + ^{nat}\text{U}$  36 A.MeV system were noticeably modified as compared to previously published data [28] (see accompanying paper [31]).

A  $^{155}\text{Gd}$  beam accelerated by the GANIL cyclotrons was used to bombard a 100  $\mu\text{g}/\text{cm}^2$  U target, enclosed between two 20  $\mu\text{g}/\text{cm}^2$  carbon layers. In order to ensure a negligible rate of multiple interactions in the target, the

beam intensity was maintained around  $3 \times 10^7$  pps. The low target thickness was chosen to allow slow fragments to escape the target. Due to the high detection efficiency of the CsI for  $\gamma/e^-$ , a minimum-bias trigger based on the multiplicity of fired modules was chosen. Two settings were used: first  $M \geq 4$  and then  $M \geq 8$  in order to minimise the proportion of triggering events which involve the carbon backings. Only runs using the  $M \geq 8$  trigger are analysed here. In the off-line analysis, events having a multiplicity of correctly identified charged particles inferior to the experimental trigger condition were rejected for reasons of coherency (with the exception of Fig. 2).

### 3 Event selection methods and procedures

#### 3.1 Removal of poorly measured events from the data sample

As a first step in our event selection procedure, we seek to exclude from the data sample poorly-measured events, i.e. ones for which a complete detection of all reaction products has not been achieved. This is necessary for two reasons. First of all, we want to characterise those rare events for which a composite system containing almost all of the mass of the colliding nuclei undergoes multifragmentation. Secondly, it is an essential prerequisite for the analyses using global variables that we will use later. In the case of the  $^{155}\text{Gd} + ^{\text{nat}}\text{U}$  reaction, a way must also be found to eliminate reactions of the projectile with the carbon target backing.

The degree of confidence with which we can judge the analysed events to be ‘complete’ increases with the total detected charge and momentum (Fig.2). Indeed, without making any hypothesis about the physics of the studied reactions, with a 100% -perfect detection one should measure the total system charge ( $Z_{\text{sys}} = Z_{\text{proj}} + Z_{\text{targ}} = 64 + 92 = 156$ ) and the beam momentum ( $P_{\text{proj}}$ ) in the exit channel for every event. Fig.2 shows that experimentally this is far from being the case. It should be noted that the ‘momentum’ used here is calculated from the product of atomic number  $Z$  and velocity component in the beam direction  $v_z$ , and normalised to the incident (projectile) ‘momentum’ :

$$\frac{P_{\text{tot}}}{P_{\text{proj}}} = \frac{\sum Z v_z}{Z_{\text{proj}} v_{\text{proj}}} \quad (1)$$

This procedure is used to compensate for the fact that INDRA does not permit isotopic identification for fragments  $Z \geq 4$ , and neutrons are not detected. Simulations of central collisions for the highly neutron-rich  $^{155}\text{Gd} + ^{\text{nat}}\text{U}$  system including the effect of secondary particle emission show that this ‘charge momentum’ is conserved to around 96% , with a r.m.s. deviation of  $\approx 2\%$  .

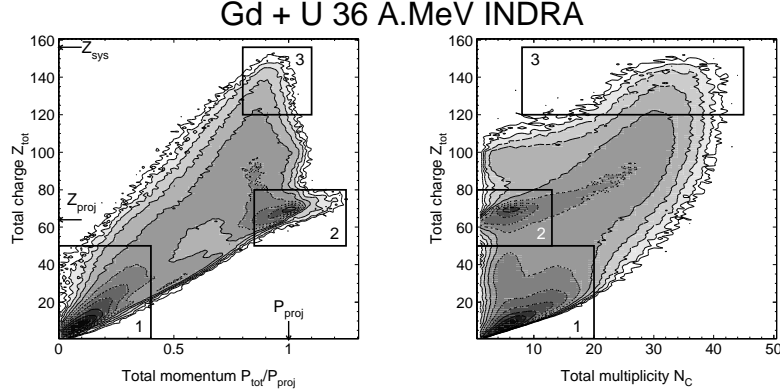


Fig. 2. *Non-equidistant logarithmic contour plots showing event-by-event correlations between the total detected charge  $Z_{tot}$ , ‘momentum’  $P_{tot}$  and multiplicity of charged products  $N_C$ . The numbered boxes correspond independently to the three classes of events discussed in the text.*

The numbered boxes in Fig.2 correspond to different classes of detected events. The design of the INDRA detector was optimised for the study of multifragmentation, typically high-multiplicity ( $\lesssim 50$ ) events in which reaction products are emitted over a large angular range. On the other hand, less violent collisions are not so well detected due to :

- (1) identification thresholds (see Sec.2) which exclude heavy, slow-moving target residues because of incomplete identification;  
and
- (2) loss of rapid projectile-like fragments at laboratory angles smaller than  $2^\circ$ .

Box 1 events mainly correspond to rather peripheral collisions for which neither projectile- (QP) nor target-like (QT) heavy fragments were detected, only light charged particles (LCP,  $Z = 1, 2$ ) and occasionally fission fragments from the target, the latter having very low energies which only permit an approximate identification via a minimum atomic number  $Z_{min}$  (see Sec.2). Most of the events in box 2 have total charge  $Z_{tot} \approx 70$  and total momentum close to that of the projectile nuclei. They correspond either to the detection of a QP and some light particles or to close-to-complete detection of  $^{155}\text{Gd}+^{12}\text{C}$  collisions in reverse kinematics. For total detected charge  $Z_{tot} > 70$  reactions with the carbon target support are completely excluded. For measured  $Z_{tot}$  values upwards of 50% of the total charge of the system  $^{155}\text{Gd} + ^{nat}\text{U}$ , increasing ‘charge-completeness’ basically leads to a global increase of the number of detected products without much change to the type of reactions observed (except for low-multiplicity events where the principal detected nuclei are a quasi-projectile and the target fission fragments).

Because of a lower overall efficiency for fragment detection compared to LCP, and trivially because of fragments’ larger atomic numbers, the requirement of

highly charge-complete events slightly favours events where a larger proportion of the available charge is detected in the form of fragments at the expense of light charged particles (see Fig.3(a) and Figs.4(e),(f)). This is especially true

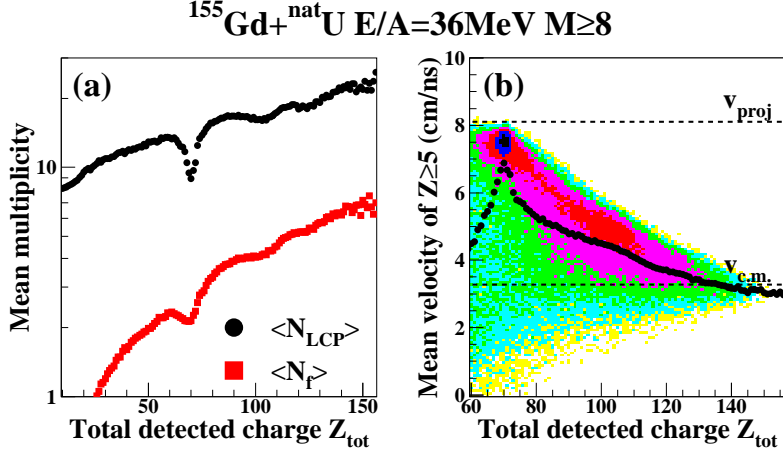


Fig. 3. Effects of the total detected charge  $Z_{\text{tot}}$  of analysed events. (a) mean multiplicities of light charged particles ( $N_{\text{LCP}}$ ) and of fragments with  $Z \geq 5$  ( $N_f$ ) as a function of  $Z_{\text{tot}}$ ; (b) weighted mean velocity of the  $Z \geq 5$  fragments (see text) versus  $Z_{\text{tot}}$ . Logarithmic intensity scale representing measured cross section. Points are the mean velocities averaged over each  $Z_{\text{tot}}$  bin.

for fragments emitted backwards in the c.m. frame, because of the increase in effective thresholds at large laboratory angles due to the recoil of the c.m. . Thus the weighted mean velocity of fragments  $\sum m_i v_i / \sum m_i$  is much larger than the  $^{155}\text{Gd} + ^{\text{nat}}\text{U}$  c.m. velocity  $v_{\text{c.m.}}$  for small total detected charge, and indeed close to that of the projectile,  $v_{\text{proj}}$  (see Fig.3(b)): we saw above that in these events all the backwards-emitted (i.e. target) fragments were missed. As  $Z_{\text{tot}}$  increases the detected fragments' mean velocity decreases as more and more backwards-emitted fragments are included. In other words, those reaction products which have a low probability of detection are not present in 'incomplete' events, whereas in 'complete' events nearly all emitted fragments must have been detected, including those emitted into experimentally unfavourable regions of phase-space, and so the selection of complete events appears to favour the detection of those products.

In order to retain a reasonably-sized data sample of very well measured events, we imposed the condition  $Z_{\text{tot}} \geq 120 (\approx 0.77 Z_{\text{sys}})$  in the off-line analysis. We judged this charge-completeness to be sufficient for two reasons. Firstly, for  $Z_{\text{tot}} \geq 120$  the weighted mean velocity of detected fragments (see Fig. 3(b)) has an average value close to (within 10%) the c.m. velocity of the collisions  $v_{\text{c.m.}}$ , which is a necessary condition for all of these fragments to have been produced in the disassembly of a fused system containing most of the mass of the projectile and target. Angular distributions of fragments and LCP, event shapes and orientations (see following section) are identical for this data sam-



ple whether calculated in the reaction ( $^{155}\text{Gd} + \text{natU}$ ) c.m. frame or in the reconstructed c.m. frame. Secondly, if only events with  $Z_{tot} \geq 0.9Z_{sys}$  are considered the only significant difference is that the mean fragment multiplicity increases by  $\approx 1$ , while the size of the data sample is drastically reduced. Angular distributions and kinematical observables are unchanged. Therefore we consider that events with  $Z_{tot} \geq 120$  are on the average sufficiently well-measured to be classified as ‘complete events’ (box 3 in Fig. 2). The additional constraint on the total detected momentum,  $0.8 \leq P_{tot}/P_{proj} \leq 1.1$ , has little effect for these events.

The measured cross-section (using target thickness and incident ion flux) for complete events is 93 mb, to be compared with a calculated reaction cross-section value of  $\sigma_R = 6.5$  barns from systematics [36]. An experimental measurement of  $\sigma_R$  was not possible because of the carbon target support. If this selection seems somewhat draconian, let us recall that it is an essential condition in order to be able to correctly reconstruct the kinematics of events where a very large part of the total system has undergone multifragmentation. We will show in the following that the accuracy of this reconstruction is of paramount importance for the isolation of such events.

### 3.2 Impact parameter selectors (IPS)

How may one isolate a sample of events corresponding to the formation and multifragmentation of a single excited nuclear system? A first answer may be to reason in terms of impact parameter. The ‘fusion’ events that we are looking for must correspond to central collisions: in a low energy picture for reasons of angular momentum; in a high energy picture to maximise the participant zone.

Events may be classed into impact parameter bins using global variables which are supposed to increase (or decrease) monotonically with  $b$  and the geometrical prescription [37]:

$$b_{est}(\Phi_1) = \frac{b_{max}}{\sqrt{N_{ev}}} \sqrt{\int_{\Phi_1}^{\Phi_{max}} \frac{dN}{d\Phi} d\Phi} \quad (2)$$

Here  $\Phi$  represents the chosen global variable, in this case reaching its maximum value  $\Phi_{max}$  when  $b \rightarrow 0$ .  $N_{ev}$  is the total number of recorded events (corresponding to the total geometrical cross-section  $\pi b_{max}^2$ ), and  $b_{est}$  is the estimated impact parameter for events characterised by the value  $\Phi = \Phi_1$ . The assumption underlying Eq.( 2) is that one can assign a single impact

parameter to each value of the global variable and vice-versa, i.e. that fluctuations are negligible.

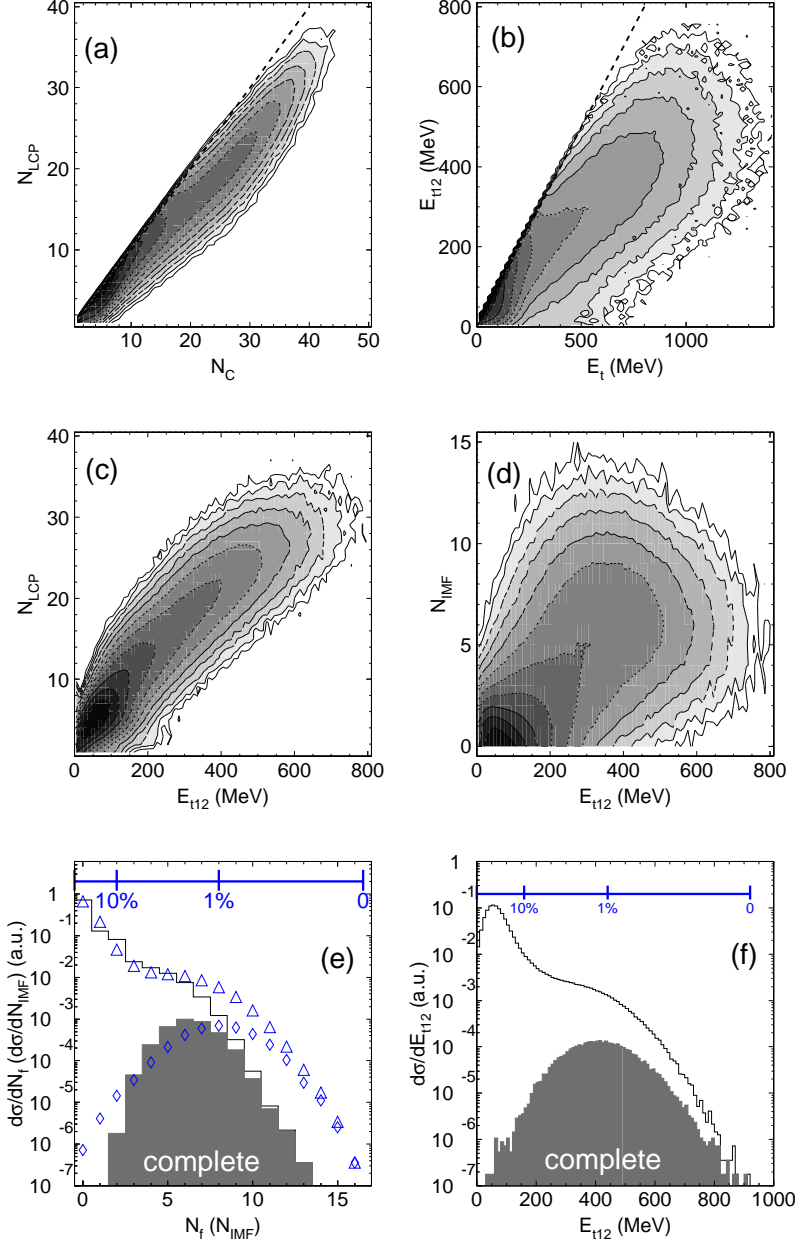


Fig. 4. (a)–(d) Non-equidistant contour plots showing event-by-event correlations between  $N_{\text{LCP}}$ ,  $N_{\text{C}}$ ,  $E_{\text{t12}}$ ,  $E_{\text{t}}$  and  $N_{\text{IMF}}$  (see text for definitions). (e) Distributions of  $N_{\text{f}}$  and  $N_{\text{IMF}}$  for all recorded events (open histogram and triangles, respectively) and for complete events (shaded histogram and diamonds, respectively). (f) Distributions of  $E_{\text{t12}}$  for all recorded events (open histogram) and for complete events (shaded histogram). An approximate scale in integrated cross-section, beginning with the ‘most central collisions’ (largest values of each IPS), is shown in percent for the two variables  $N_{\text{IMF}}$  and  $E_{\text{t12}}$ .

The most often-used IPS variables are multiplicities (total multiplicity  $N_{\text{C}}$ ,

LCP multiplicity  $N_{\text{LCP}}$ ) and total transverse energies (of all particles  $E_t$ , or uniquely LCP  $E_{t12}$ ). In addition we have defined the multiplicity of ‘intermediate mass fragments’ (IMF) to be the number of nuclei with  $3 \leq Z \leq 30$  ( $N_{\text{IMF}}$ ), and the multiplicity of fragments  $N_f$  for products with  $Z \geq 5$ . Panels (a)–(d) of Fig.4 present event-by-event correlations between these variables. One may first note the large spread of values around the mean correlation in each case, therefore fluctuations cannot be neglected, as has often been observed for dissipative collisions in and below the Fermi energy range. Each IPS will thus share events differently between estimated impact parameter bins. On the other hand the effect of fluctuations on Eq.( 2) is to underestimate the impact parameter for the 10% most central collisions [37–39]. On Fig. 4 approximative integrated cross-sections are shown for  $N_{\text{IMF}}$  and  $E_{t12}$  which are calculated with respect to the total number of recorded events, irrespective of  $Z_{\text{tot}}$ . As this number includes reactions between the beam and the carbon target backings (see Sec. 3.1) the percentages given are a lower limit. Complete events therefore belong to the  $\geq 10\%$  most central  $^{155}\text{Gd} + ^{\text{nat}}\text{U}$  collisions measured (Fig.4(e) & (f)) and further ‘impact parameter selection’ e.g. multiplicity cuts may well be ineffectual.

Let us mention in passing the variable  $Z_{\text{bound}}$  used by the Aladin collaboration [40,12]. It corresponds to the sum of atomic numbers of all fragments with  $Z \geq 2$ . In collisions between 100A.MeV and 1AGeV using the Aladin spectrometer  $Z_{\text{bound}}$  represents the size of the projectile spectator minus evaporated hydrogen isotopes. In this energy range the near-geometrical dependance of spectator size on impact parameter makes  $Z_{\text{bound}}$  a good IPS. The variable  $Z_{\text{bound}}$  does not behave as an IPS with the complete detection of particles and fragments from both target and projectile. In another context, it can be useful for model comparisons if it is defined to be the total charge of all fragments (e.g. with  $Z \geq 5$ ) when comparing data with calculations whose principal aim is to reproduce fragment partitions but not all the LCP emitted at different stages of the reaction (see accompanying paper [31]). For complete events of  $^{155}\text{Gd} + ^{\text{nat}}\text{U}$  the average value of the total charge contained in fragments  $Z \geq 5$  corresponds to approximately 50% of the total system charge.

### 3.3 Global shape variables (GSV)

A more direct method of discriminating between different reaction mechanisms is based on considering how fragments are distributed in the centre of mass momentum or velocity space on an event-by-event basis (the ‘event shape’) [41]. We carry out this analysis using fragments with  $Z \geq 5$  rather than the more usual  $Z \geq 3$  definition because of the very heavy nature of the system (note that both definitions are quite arbitrary). LCP are left out of the analysis as they result from several different mechanisms not directly related to fragment

production (e.g. pre-equilibrium emission, evaporation from hot fragments) and also their smaller masses can blur event shapes in velocity space. Then the formation of ‘fused systems’ containing most of the incident nucleons is characterised by isotropic emission of fragments in the centre of mass frame, assuming for simplicity complete relaxation of the multifragmenting system’s form i.e. a spherical source, and negligible angular momentum (spin). On the other hand the existence of two principal moving sources of emission (e.g. the two partners of a deeply-inelastic collision), or of spectator-like fragments separating from some ‘participant zone’ around mid-rapidity, implies a rod-like elongated event shape. The variables used to exploit this difference in event shape come from high-energy particle physics, where pattern recognition in momentum distributions has long been a major concern [42].

From the cartesian components of fragment ( $Z \geq 5$ ) momenta in the centre of mass one may construct the tensor [43],

$$Q_{ij} \equiv \sum_{Z \geq 5} \frac{p_i p_j}{2m} \quad (3)$$

whose eigenvectors and eigenvalues may be interpreted in terms of an ellipsoid in momentum space, and which give information on both the event shape (sphericity, coplanarity etc.) and its orientation with respect to the beam (see Fig.5, upper panels). If  $\{\lambda_1, \lambda_2, \lambda_3\}$  are the eigenvalues of Eq.(3), normalised

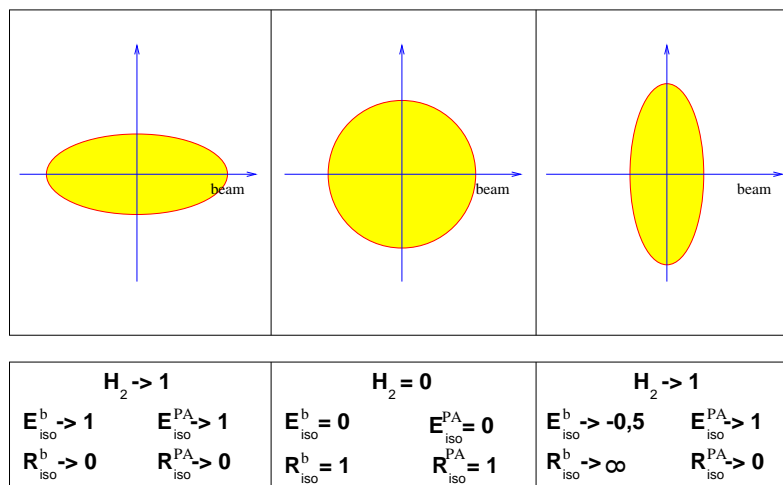


Fig. 5. Values of global shape variables (GSV) for different event-shapes (represented by an ellipse) and orientations with respect to the beam axis. ‘b’ and ‘P.A.’ refer to variables calculated with respect to the beam axis or the principal axis of the event, respectively. It should be noted that spherical event shapes (central panel) can only be achieved for very high (infinite) multiplicities.

to their sum and labelled according to increasing size,  $\lambda_3 \geq \lambda_2 \geq \lambda_1$ , then

$$\text{sphericity } S = \frac{3}{2} (1 - \lambda_3) \quad (4)$$

$$\text{coplanarity } C = \frac{\sqrt{3}}{2} (\lambda_2 - \lambda_1) \quad (5)$$

The ‘flow axis’ corresponding to the largest eigenvalue  $\lambda_3$ , or major axis of the ellipsoid, defines the principal axis of the event, whose deviation from the beam is referred to by the polar angle  $\theta_{\text{flow}}$ . This angle varies between  $0^\circ$  and a maximum value of  $90^\circ$  because, by convention, it is taken as the angle between the forward lobe of the ellipsoid and the beam. For events which have lost all memory of the entrance channel kinematics (e.g. single-source events with negligible angular momentum) this angle is isotropically distributed, whatever the fragment multiplicity. In the case of a single source with large angular momentum all angles are populated but directions close to the beam are favoured [39], due to the preferential emission of fragments in the reaction plane.

Independently of the tensor one may construct other shape-dependent variables, for example : the second moment of Fox and Wolfram,  $H_2$  [44]

$$H_2 = \frac{H(2)}{H(0)} \quad (6)$$

$$= \frac{1}{H(0)} \sum_{1,2} \frac{1}{2} |\vec{p}_1| |\vec{p}_2| (3 \cos^2 \theta_{rel} - 1), \quad (7)$$

$$H(0) = \sum_{1,2} \frac{1}{2} |\vec{p}_1| |\vec{p}_2| \quad (8)$$

where the sums are over pairs of fragments,  $\vec{p}_1, \vec{p}_2$  are their c.m. momenta, and  $\theta_{rel}$  is their relative angle; the momentum isotropy ratio,  $R_{\text{iso}}$  [45],

$$R_{\text{iso}} = \frac{2}{\pi} \left( \sum |\vec{p}_\perp| / \sum |\vec{p}_\parallel| \right) \quad (9)$$

where the sums are over all fragments, and  $\vec{p}_\perp, \vec{p}_\parallel$  represent perpendicular and parallel projections of  $\vec{p}$ ; and an energy isotropy ratio such as  $E_{\text{iso}}$  [46],

$$E_{\text{iso}} = 1 - \frac{3}{2} \left( E_\perp / \sum_i E_i \right) \quad (10)$$

$$E_\perp = \sum_i E_i \sin^2 \theta_i \quad (11)$$

where the sums are again over fragments,  $E_i$  is the c.m. kinetic energy of the  $i^{\text{th}}$  fragment, and  $\theta_i$  its polar angle. An alternative choice, with a slightly different definition, is the variable  $ERAT$  used by the FOPI collaboration [47].

By construction  $H_2$  is independent of the choice of basis axes in the c.m. momentum space (it only depends on relative angles between pairs of fragments), whatever the event shape. The values of  $E_{\text{iso}}$  and  $R_{\text{iso}}$  for spherical events are also independent of the choice of axes. However, spherical events require infinite multiplicities of fragments even if the latter are isotropically emitted, and so are never observed [48]. This is because the event-shape deduced from a small number of isotropically-emitted fragments is only a poor approximation to the ‘true’ spherical distribution, due to the extremely restricted sampling of the available momentum space event by event. As Fig.5 shows, because the event shape is always non-spherical  $E_{\text{iso}}$  and  $R_{\text{iso}}$  have to be calculated with respect to the principal axis of the event in order to ensure non-ambiguous shape determination. When calculated with respect to the beam axis their values depend not only on the event shape but also its orientation in the velocity space,  $\theta_{\text{flow}}$ . In the following we will implicitly suppose that isotropy ratios are calculated unambiguously, unless explicitly stated otherwise.

The effectiveness of event-shape discrimination is weakened by the fact that we cannot unambiguously define what values of the GSV should correspond to the formation and decay of fused systems because for small multiplicities the event-shape depends strongly on the number of emitted fragments. On the other hand, an isotropic distribution of flow angles for a set of events is an unambiguous signal which is independent of the fragment multiplicity that fragments have lost all memory of the entrance channel. This fact will be exploited in the following section in order to select single-source events.

Fig.6 presents some experimental correlations of these global shape variables for complete events (an event-shape analysis has no sense unless performed for complete events). Fig. 6(a) shows the correlation between a global shape variable,  $R_{\text{iso}}$ , and an impact parameter selector,  $E_{\text{t12}}$ . Two regions are apparent: one corresponding to very elongated events and quite large impact parameters ( $R_{\text{iso}} < 0.25$ ,  $E_{\text{t12}} < 300$  MeV); the other covering a very broad range of both event shapes and transverse energies. The former set of events are the least dissipative collisions which are sufficiently violent in order to be well-measured i.e. which are not excluded by the requirement of complete events. We will see in the next section that the principal products of these reactions are residues of the quasi-projectile and of the target fission fragments which are well-separated in velocity space. As for the remaining events, they correspond to strongly dissipative collisions and it should be noted that the event shape and impact parameter observables show no strong correlation. We will show the existence of ‘fusion’ i.e. single-source events for a fraction of these collisions in the following section.

Figs.6(b) and (c) show the experimental correlations which exist between the three GSV. All of them well separate the two classes of events remarked in Fig.6(a), especially  $H_2$ .  $E_{\text{iso}}$  shows a greater variation than  $H_2$  for the most

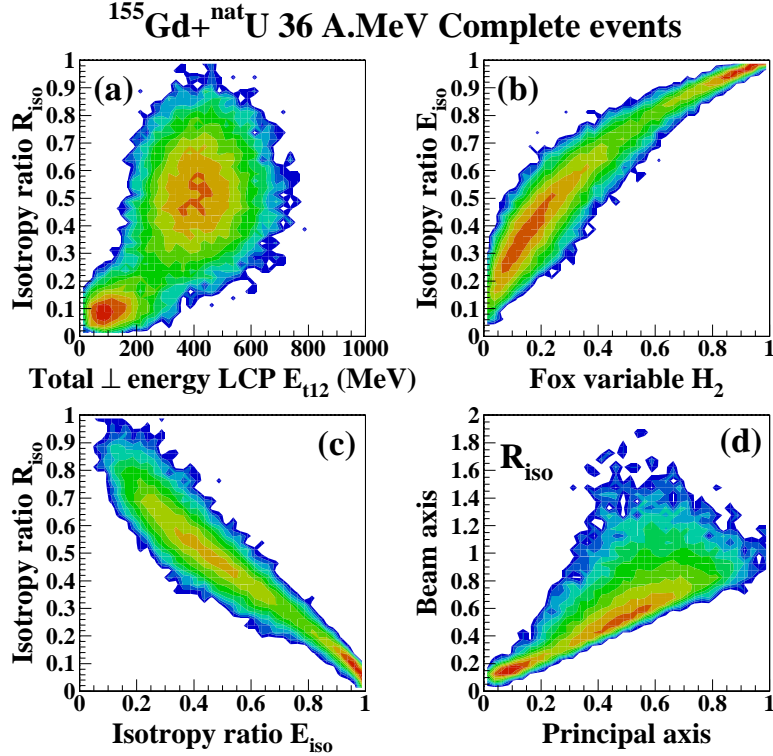


Fig. 6. *Event-by-event correlations, for complete events, between: (a) event-shape ( $R_{\text{iso}}$ ) and impact parameter selector  $E_{t12}$ ; (b)  $E_{\text{iso}}$  and  $H_2$ ; (c)  $R_{\text{iso}}$  and  $E_{\text{iso}}$  (isotropy ratios calculated with respect to the principal axis of each event); (d)  $R_{\text{iso}}$  calculated with respect to the beam axis and with respect to the principal axis of each event.*

dissipative collisions, which may mean that it has a greater sensitivity to variations among very compact event-shapes. On the other hand the two isotropy ratios, calculated from fragment momenta or kinetic energies, are very strongly correlated and may be considered to give equivalent information on event shapes.

Finally in Fig.6(d) we present the correlation between the values of the isotropy ratio  $R_{\text{iso}}$  calculated with respect to the beam axis (‘ambiguous’ shape variable) or the principal axis of the event (‘unambiguous’ shape variable). For the most elongated event shapes (small  $R_{\text{iso}}$ ) the two methods of calculating  $R_{\text{iso}}$  give very similar values, because the least dissipative events have mean  $\theta_{\text{flow}}$  angles of  $\approx 10^\circ$  (see Fig.7), therefore the principal axis and the beam axis are almost aligned. The majority of the more compact events (principal axis isotropy ratio  $> 0.25$ ) also have axis-independent isotropy ratios (crest following a line “beam axis  $R_{\text{iso}} = \text{principal axis } R_{\text{iso}}$ ”), and this is once again because  $\theta_{\text{flow}}$  remains quite small for these events (Zone 2 of Fig.7).

However there are also events for whom the isotropy ratio (i.e. the apparent

event shape) depends strongly on the axis chosen, for example appearing as “spherical” ( $R_{\text{iso}} = 1$ ) with respect to the beam axis but non-spherical ( $R_{\text{iso}} < 1$ ) with respect to the principal axis of the event. Note also the existence of events for whom the isotropy ratio with respect to the beam axis  $R_{\text{iso}} > 1$ , which implies an event shape elongated perpendicular to the beam direction. In both of these cases the ‘ambiguous’ apparent event shape is due to the increase of  $\theta_{\text{flow}}$ , which modifies the projection of the fragment momenta on to the beam axis. For a given unambiguous  $R_{\text{iso}}$  approaching 1, the truly increasingly spherically-symmetric events populate ‘beam axis event shapes’ which vary less and less with  $\theta_{\text{flow}}$ , as one would expect. However we do not observe an ‘island’ of truly spherical events with  $R_{\text{iso}}^{\text{beam}} = R_{\text{iso}}^{\text{P.A.}} = 1$ . Once again this is because for the fragment multiplicities in play, a spherical event shape can not be attained due to finite number effects, even if all fragments are emitted isotropically.

#### 4 Event classification using the ‘Wilczyński diagram’: isolation of single-source events

In order to classify  $^{155}\text{Gd} + ^{\text{nat}}\text{U}$  36 A.MeV collisions we use a method which was first employed for the analysis of Pb+Au 29 A.MeV reactions studied with the multidetector Nautilus [23]. The correlation between total measured c.m. kinetic energy of detected charged products (TKE) and the principal direction of fragment ‘flow’ ( $\theta_{\text{flow}}$ ) when plotted for each event (see Fig. 7) resembles the Wilczyński diagram [49] well-known at bombarding energies below 20 A.MeV. TKE provides a dissipation scale for the collisions, decreasing as more and more excitation energy is deposited in the system. For complete events we may write

$$\text{TKE} = E_{c.m.} + Q - \sum E_{\text{neutron}} - \sum E_{\gamma} \quad (12)$$

where  $E_{c.m.}$ ,  $Q$ ,  $\sum E_{\text{neutron}}$  and  $\sum E_{\gamma}$  are, respectively, the available centre-of-mass energy, the mass balance of the reaction and the total neutron and gamma ray kinetic energies. The increase of  $E^*$  with increasingly dissipative collisions implies higher average multiplicities and energies of neutrons, light charged particles, and fragments : the latter account for an increasingly negative mass balance.

Just as at low energy (for heavy systems), a dog-legged correlation appears with a crest running from forward-peaked, slightly dissipative collisions (large TKE) to highly-damped reactions with little or no memory of the entrance channel (large  $\theta_{\text{flow}}$ ). We have defined four classes of events depending on their position in the ‘Wilczyński diagram’, Fig.7. In order to examine the topology



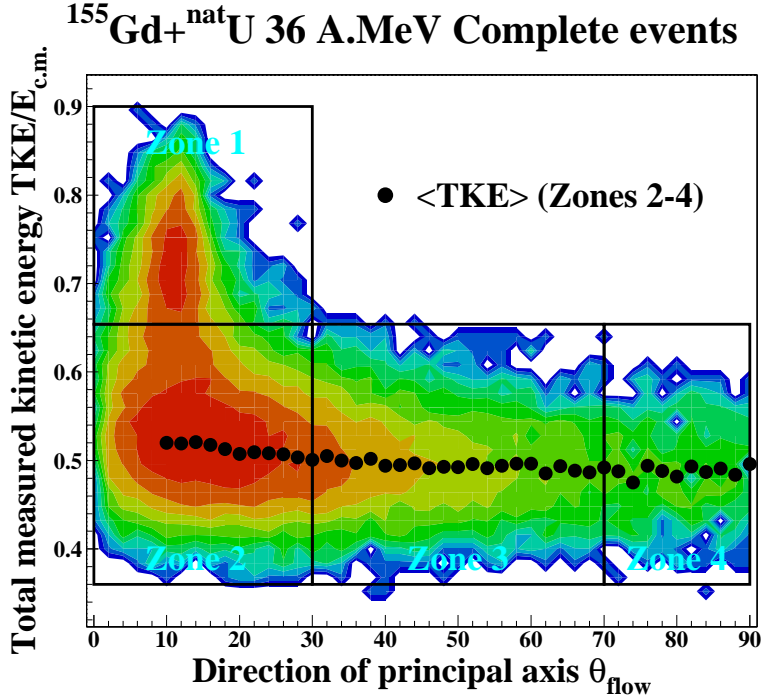


Fig. 7. ‘Wilczyński diagram’ for complete events: logarithmic intensity scale representing measured cross-section as a function of total measured c.m. kinetic energy (as a fraction of the available centre of mass energy) and ‘flow’ angle or direction of the event principal axis,  $\theta_{\text{flow}}$ . The four zones indicated are used to classify complete events (see text). For events in Zones 2 to 4 the mean value of TKE is indicated (points) for each  $\theta_{\text{flow}}$  bin.

of the fragment emission in velocity space in each class of events, we present the charge-velocity correlations for each Zone, Fig.8. Here, as a function of velocity along the beam axis or the principal axis of each event, the average charge density of fragments is reported, which we define as the average charge of all the fragments with  $Z \geq 5$  which fall in a given bin in parallel velocity, normalised to the width of the bins. This is a simplified version of the tool first presented in [50]. The distributions of Fig.8 therefore give an insight into the repartition in velocity space of the charge bound in fragments.

In Zone 1 are found the least dissipative collisions which are sufficiently violent in order to be well measured. The direction of the principal axis for these events remains close to the grazing angle ( $\theta_{gr}^{c.m.} = 9.8^\circ$  [36]), and the principal reaction products are residues of the quasi-projectile ( $v \approx 4.5$  cm/ns) and of the target fission fragments ( $v \approx -2$  cm/ns and  $-4.5$  cm/ns, respectively). Let us note in passing that although Fig.8(a) shows clearly that the majority of charge bound in fragments is concentrated in projectile- and target-like products, the velocity space between projectile and target (the so-called mid-rapidity region) is not empty but populated by a few intermediate mass fragments which may result from the decay of a ‘neck’ of matter between the two principal partners

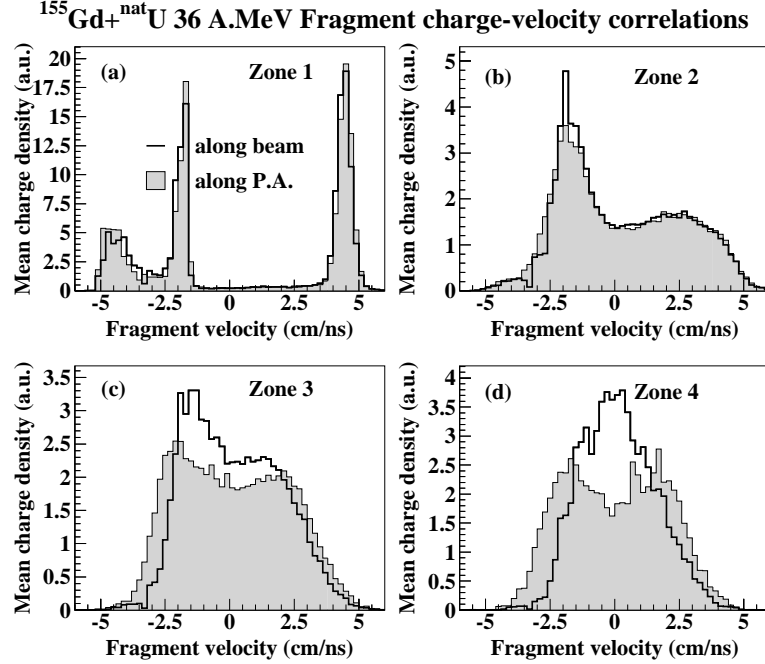


Fig. 8. Fragment charge-velocity correlations for the four classes of events corresponding to the zones defined in the Wilczyński diagram (Fig.7). The mean charge density (see text) is plotted as a function of the velocity parallel to the beam axis (thick lines) or the principal axis, P.A., of each event derived from the tensor Eq.3 (shaded histograms).

of the reaction, as has been observed for mid-central collisions of other heavy systems around the Fermi bombarding energy (see for example [19–21,13]).

The most dissipative collisions (Zones 2 to 4) populate all  $\theta_{\text{flow}}$  angles, although in majority events are still concentrated at small angles,  $\theta_{\text{flow}} < 30^\circ$  (Zone 2 in Fig.7). The  $\cos \theta_{\text{flow}}$ -distribution becomes flat (isotropic) for large flow angles (Fig.9(a)). The repartition of the fragments' charge is more homogeneous than in Zone 1: specifically, the mid-rapidity region is fully populated. However, in Zone 2 (Fig.8(b)) there are two asymmetric ‘bumps’ in the distribution at forward and backward velocities, strongly reminiscent of the entrance channel. Although not strictly correct, we will refer to this type of fragment emission topology as ‘binary’ events in the following. In Zones 3 and 4 (Fig.8(c) and (d)), due to the increasing deviation of the principal axis from the beam direction,  $\theta_{\text{flow}}$ , the charge density is not distributed in the same way according to one or the other axis. Thus, with respect to the beam direction, the two components' relative velocity becomes smaller in Zone 3 than in Zone 2 while in Zone 4 only one component peaked at the c.m. velocity is seen; on the other hand, in the velocity-space along the principal axis, two components are present whatever the Zone and their relative velocity decreases only very slightly while the distribution becomes symmetric with regard to the c.m. velocity.

This result is difficult to interpret. The distributions with respect to the beam axis suggest that as  $\theta_{\text{flow}}$  increases fragments are produced in the break-up of increasingly relaxed projectile- and target-like primary fragments, giving way to fusion-like reactions for  $\theta_{\text{flow}} \geq 70^\circ$ . However, this would be in contradiction with the fact that the mean TKE of events in Zones 3 and 4 is constant, and only slightly lower than in Zone 2 (Fig.7, points). The energy dissipated in the collisions is practically constant for Zones 2 to 4, which is, on the other hand, consistent with the velocity distributions with respect to the principal axis of each event. One can then understand the apparently spurious evolution of the two components' relative velocity along the beam direction to be due to the effect on the projections on to the beam axis of increasing  $\theta_{\text{flow}}$ .

Does this then mean that fragments in Zone 4 result from the break-up of projectile- and target-like primary fragments, moving apart almost perpendicularly to the beam ? This is not so clear, as in fact both distributions of Fig.8(d) are compatible with the break up of a fused system in to a small number of fragments. This is because event-shapes for low-multiplicity reactions are never spherically symmetric (see Sec.3.3), therefore one can always define event-by-event an oriented principal axis. In the case of the isotropic break-up of a fused system the principal axis has no physical significance and can take all directions, therefore angular distributions with respect to the beam are isotropic. On the other hand the principal axis lies by definition in the direction of maximum elongation of each event shape, therefore with respect to this axis fragments seem to be preferentially emitted in the forward and backward directions, with equal probability [39]. Thus Fig.8(d) does not permit to conclude on the origin of the fragments, and we must examine their characteristics in greater detail.

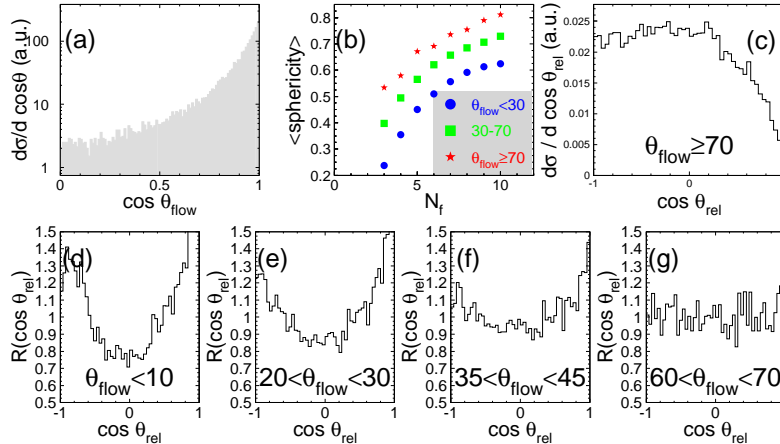


Fig. 9. For the most dissipative collisions (Zones 2–4 of Fig.8): (a) ‘flow’ angle distribution; (b) mean sphericity of the events as a function of the fragment multiplicity  $N_f$ ; (c) distribution of relative angles  $\theta_{\text{rel}}$  between pairs of fragments in Zone 4 events; (d)–(g) evolution of fragment-fragment relative angle distributions with  $\theta_{\text{flow}}$ , each distribution has been divided by the distribution for Zone 4 events.

Mean event-shape sphericity as a function of fragment multiplicity is shown in Fig.9(b) for the three Zones in  $\theta_{\text{flow}}$  corresponding to the most dissipative collisions (Zones 2–4). One should first of all note that for each class of events the increase of sphericity with fragment multiplicity is expected from the finite number effects we discussed above. We see that in general event sphericity increases with ‘flow’ angle, and that for each fragment multiplicity the most compact events are found in Zone 4 ( $\theta_{\text{flow}} \geq 70^\circ$ ). This is a strong signal of the evolution of fragment kinematics towards single-source emission, as : (i) the event sphericity and  $\theta_{\text{flow}}$  are *a priori* independent observables; and (ii) only comparisons of event shapes for constant multiplicity avoid distortions due to the aforementioned finite number effects.

One may examine in more detail this evolution by looking at the distributions of relative angles ( $\theta_{\text{rel}}$ ) between pairs of fragments emitted in the same event. Fragments emitted by the same source have an isotropic distribution of  $\theta_{\text{rel}}$  angles in the rest frame of the emitter, except for small  $\theta_{\text{rel}}$  which are suppressed by Coulomb repulsion between nascent fragments in the case of rapid successive emissions. Fig.9(c) shows exactly this type of distribution for fragment-fragment relative angles in the Zone 4 events, which are therefore compatible with the fast break-up of a single source. Figures 9(d)–(g) show the evolution of the relative angle distributions with the flow angle of the events. In each case, the distribution has been divided by that of the Zone 4 events (Fig.9(c)), in order to highlight any differences between the two event samples (a value of 1 for all angles means that the considered distribution is identical to that for Zone 4 events). The fact that small and large relative angles between fragment pairs are favoured compared to Zone 4 in events with  $\theta_{\text{flow}} < 10^\circ$  (Fig.9(d)) reveals the dominance of emission from two distinct sources moving apart in the c.m. frame in these events: large relative angles are populated by fragment pairs coming from different sources, while the repopulation of small relative angles is due to kinematical focusing in the direction of the source velocity of fragments born of the same source. The decreasing relative population of large and small angles when increasing the flow angle of the events reflects the diminishing importance of collisions leading to projectile- and target-like primary fragments. It should be noted that relative angle distributions such as that shown in Fig.9(f) can also be obtained if fragments are emitted from a spherical source having very large angular momentum [39].

To summarise the results presented in this section, we have shown that the ‘Wilczyński diagram’ (Fig.7) allows to sort well-measured reactions in to classes of events (‘Zones’) according to the total measured kinetic energy in the c.m. frame TKE and the flow angle  $\theta_{\text{flow}}$ . We have presented the evolution of these reactions from the least violent collisions, where fission of the target nucleus is observed, to highly dissipative ‘binary’ collisions, in which many fragments are produced but they retain a strong kinematical memory of the projectile-target asymmetry. This evolution concerns the first three Zones of

the ‘Wilczyński diagram’. In Zone 4 are found events for which : (i) no memory of the entrance channel remains; (ii) no projectile- or target-like fragments are observed; (iii) mean event shapes are the most compact of all the very dissipative collisions; (iv) fragment kinematics are consistent with rapid emission from a single source; (v) moreover this single source must contain a very large proportion of the available mass and energy i.e. preequilibrium emission is limited (otherwise for an asymmetric system in direct kinematics one would expect the ‘fused’ system to recoil with a velocity less than that of the system centre of mass, cf. Fig. 8(d)) [51].

The ‘Wilczyński diagram’ therefore permits the isolation of a sample of single-source events for  $\theta_{\text{flow}} \geq 70^\circ$ . Let us recall that for single-source events the flow angle takes all values, therefore single-source events must also be present for  $\theta_{\text{flow}} < 70^\circ$ . However as we have seen, events with small  $\theta_{\text{flow}}$  are dominated by a ‘binary’ fragment emission topology, and keep a strong memory of the entrance channel. Only at large flow angles do single-source events become dominant and separable using a  $\theta_{\text{flow}}$  cut. Of course, this selection method can only function if the flow angle retains a memory of the direction of the primary projectile- and target-like fragments coming from highly dissipative binary reactions, and this direction must remain close to the beam axis. It is possible that this may only occur for heavy systems, for which binary highly dissipative collisions are strongly focused around the grazing angle due to Coulomb effects [23,25]. If binary collisions of light systems lead to large flow angles even with low cross-sections then single-source events, when present, may not be revealed by a  $\theta_{\text{flow}}$ -cut. Other more refined selection methods must be applied [52] in this case.

To conclude this section we will give an estimate for the cross-section associated with the formation and multifragmentation of fused systems for  $^{155}\text{Gd} + ^{\text{nat}}\text{U}$  36 A.MeV reactions. The measured cross-section for events in Zone 4 is 2.6 mb, which is  $\approx 3\%$  of the total cross-section for complete events. Now we must estimate the fraction of all single-source events represented by this sample taking into account (i) the  $\theta_{\text{flow}}$  selection and (ii) the selection of complete events.

If all the single-source events have an isotropic flow angle distribution the fraction of these events that we have selected is given by  $\cos 70^\circ = 0.34$ . This is the case assuming the formation of spherical fused systems with negligible angular momentum. In a less ideal scenario we should allow for deformed and/or turning fused systems formed at finite impact parameters. The  $\cos \theta_{\text{flow}}$ -distribution in this case would be forward-peaked [53] and the fraction of single-source events retained by the  $\theta_{\text{flow}}$  cut would therefore be less than 34%. This fraction must however be much greater than 3% (fraction of all complete events found in Zone 4) because Zone 2 and Zone 3 events are clearly not dominated by single-source events. Let us suppose as a conservative estimate

that Zone 4 events correspond to 20% of all single-source events. We will use this as an upper estimate for the total cross-section. As a lower estimate we will suppose that the  $\theta_{\text{flow}}$ -distribution is indeed isotropic and that the Zone 4 event sample is polluted by ‘binary’ events. Given the characteristics of these events presented above we think that an upper estimate for this pollution is around 10% .

As far as the selection of complete events is concerned, these single-source multifragmentation events belong to the class of very violent collisions for which the efficiency of the INDRA detector array is optimal. However the geometrical efficiency of 90% is perhaps not attained due to the very high multiplicities of these events (double hits). The distribution of  $Z_{\text{tot}}$  for Zone 4 events is a monotonously decreasing function of  $Z_{\text{tot}}$  (it is of course truncated at  $Z_{\text{tot}} = 120$  because of our complete events selection) and can be fitted by the tail of a gaussian function of mean value  $\langle Z_{\text{tot}} \rangle = 115$  and width  $\sigma = 13$ . We estimate the fraction of all single-source events retained by the complete-event selection to be the fraction of the area under this gaussian curve contained between the limits  $Z_{\text{tot}} = 120$  and  $Z_{\text{tot}} = 156$  which we found from numerical integration to be 37% .

With these hypotheses we can estimate an upper limit for the total single-source cross-section (assuming a deformed spinning source, assuming the Zone 4 sample to be free of ‘pollution’ and correcting for event completeness) to be

$$\sigma_{1\text{source}}^{\text{max}} = 2.6\text{mb} \times \frac{1}{20\%} \times \frac{1}{37\%} = 35\text{mb} \quad (13)$$

while a lower limit (assuming a pollution of Zone 4 by binary events, assuming only spherical zero-spin fused systems and correcting for event completeness) is given by

$$\sigma_{1\text{source}}^{\text{min}} = 90\% \times 2.6\text{mb} \times \frac{1}{34\%} \times \frac{1}{37\%} = 19\text{mb} \quad (14)$$

Let us remark that if one makes the extreme assumption that all of the most dissipative complete events are compatible with the multifragmentation of deformed single sources [54] (3% instead of 20% in Eq. (13)) then the upper limit for the cross section associated with the multifragmentation of fused systems would be estimated to be 234 mb ( $\approx 3\%$  of the total reaction cross section).

## 5 Can single-source events be isolated using other selection methods ?

We have shown how a sample of single-source events may be isolated based on the degree of rotation of the event ellipsoid,  $\theta_{\text{flow}}$ . This sample represents at most 34% of all the single-source events present among the most dissipative events. One might wonder if another approach, perhaps based on the more commonly-used tools of impact parameter selection or event-shape discrimination discussed in Sec.3.2 and Sec.3.3, would not be better adapted to isolate a larger data sample e.g. by including the small- $\theta_{\text{flow}}$  single-source events ? With this goal in mind we will now look in more detail at the behaviour of IPS and GSV with regard to the ‘Wilczyński’ event classification scheme.

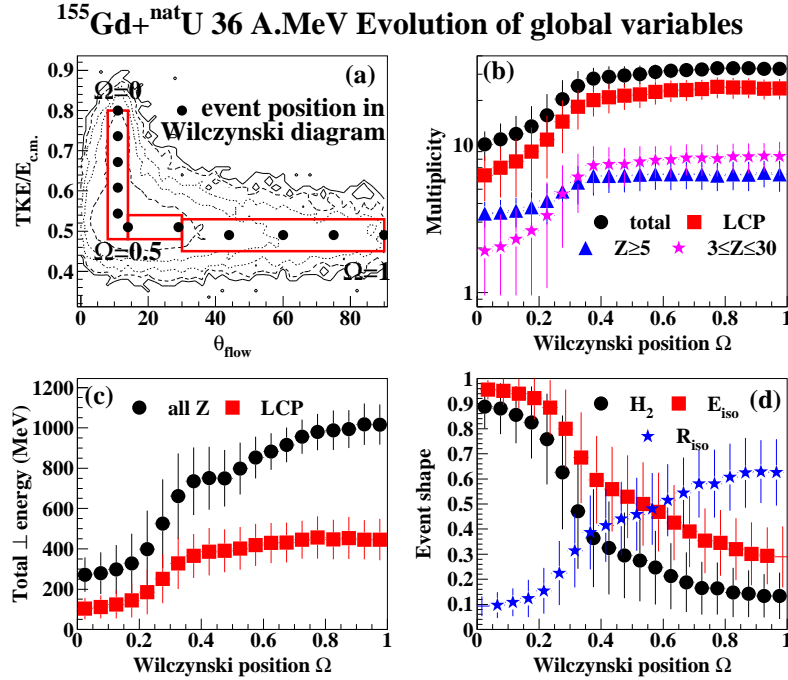


Fig. 10. (a) ‘Wilczyński diagram’ (Fig. 7) for complete events, showing the definition of the event position variable,  $\Omega$ . Points correspond to  $\Omega = 0, .1, .2, \dots$  (b) Evolution of total ( $N_C$ ), LCP ( $N_{\text{LCP}}$ ),  $Z \geq 5$  ( $N_F$ ) and  $3 \leq Z \leq 30$  ( $N_{\text{IMF}}$ ) multiplicities as a function of event position in the ‘Wilczyński diagram’. (c) Evolution of the total transverse energy of all charged products,  $E_t$ , and of LCP,  $E_{t12}$ . (d) Evolution of the event shape according to  $H_2$ ,  $E_{\text{iso}}$  and  $R_{\text{iso}}$  (the two isotropy ratios are calculated according to the principal axis of each event). Points correspond to mean values, vertical bars to standard deviations.

Fig.10 presents the evolution of the mean values of the IPS and GSV variables presented in Secs. 3.2 and 3.3 as a function of event position in the ‘Wilczyński diagram’. In order to do this we defined an observable,  $\Omega$ , which varies as a function of TKE and  $\theta_{\text{flow}}$  in such a way that it increases monotonously along

the crest of the experimental correlation observed in Fig.7 and Fig.10(a).  $\Omega$  is therefore a global variable related to the position of events in the ‘Wilczyński plot’. Its value is given by

$$\Omega = \frac{0.5}{0.32} \times \left( 0.8 - \frac{\text{TKE}}{E_{c.m.}} \right) \quad (15)$$

for  $8^\circ \leq \theta_{\text{flow}} \leq 14^\circ$  and  $0.48 \leq \text{TKE}/E_{c.m.} \leq 0.8$ , covering values  $0 \leq \Omega \leq 0.5$ , and by

$$\Omega = \frac{0.5}{76^\circ} \times (\theta_{\text{flow}} - 14^\circ) + 0.5 \quad (16)$$

for  $14^\circ < \theta_{\text{flow}} \leq 30^\circ$  and  $0.48 \leq \text{TKE}/E_{c.m.} \leq 0.54$  ( $0.5 < \Omega \leq 0.6$ ) and for  $30^\circ < \theta_{\text{flow}} \leq 90^\circ$  and  $0.45 \leq \text{TKE}/E_{c.m.} \leq 0.53$  ( $0.6 < \Omega \leq 1$ ). Outside of these limits (represented by rectangular boxes in Fig.10(a))  $\Omega$  is undefined and the corresponding event is not included in the calculated mean. Roughly speaking, events from Zone 1 of Fig.7 have  $0 \leq \Omega \leq 0.25$ ; from Zone 2,  $0.25 < \Omega \leq 0.6$ ; from Zone 3,  $0.6 < \Omega \leq 0.85$ ; and from Zone 4,  $0.85 < \Omega \leq 1$ .

It is clear that the majority of the evolution of the IPS and GSV variables takes place for  $\Omega < 0.4$  (Fig.10(b)–(d)) i.e. Zones 1 and 2 of the ‘Wilczyński diagram’, and this evolution is therefore strongly correlated to the dissipation of the available kinetic energy  $E_{c.m.}$ . We have shown that these events retain a strong memory of the entrance channel (Fig.8(a),(b) and Fig.9(d),(e)). IMF and LCP multiplicities (Fig.10(b)) as well as the total transverse energies (Fig.10(c)) all increase as the collisions become more dissipative, while event shapes become more and more compact (Fig.10(d)) reflecting the decreasing relative velocity between primary target- and projectile-like fragments in the exit channel and the increasingly isotropic emission of fragments in the c.m. frame.

If we now look to the most dissipative collisions ( $\Omega > 0.4$ : Zones 2–4 of Fig.7) the mean values of IPS variables show a slight evolution, much smaller than the standard deviations of their distributions (vertical bars in Fig.10(b)–(d)). Only  $E_t$  continues to increase significantly for  $\Omega > 0.5$  because increasing  $\theta_{\text{flow}}$  means increasing fragment transverse energies; however  $E_t$  is constant for  $\Omega > 0.8$ . The mean  $Z \geq 5$  fragment multiplicity  $N_f$  is the same whatever the position of the event in the horizontal branch of the ‘Wilczyński diagram’. It should be noted that IMF and LCP multiplicities show an identical saturation with dissipated energy, unlike what was observed for the  $^{136}\text{Xe}+^{209}\text{Bi}$  28 A.MeV reaction [55].

IPS are therefore quite insensitive to the evolution of fragment kinematics from ‘binary’ collisions to single-source events that was shown in Sec. 4, and



they seem to be most strongly correlated with energy dissipation. Let us point out that a simple calculation for heavy systems of the excitation energy per nucleon for a fully-damped pure binary collision (no mass exchange)

$$E^* = E_{c.m.} - \frac{1}{2} \frac{A_p A_t}{A_p + A_t} v_{rel}^2 \quad (17)$$

(where  $v_{rel}$  is given by the Viola systematics [56]) or for fusion

$$E^* = E_{c.m.} + \Delta(A_p, Z_p) + \Delta(A_t, Z_t) - \Delta(A_p + A_t, Z_p + Z_t) \quad (18)$$

(where  $\Delta(A, Z)$  is the mass excess of nucleus  ${}^A_Z X$ , using the extrapolation of [57] in the case of the fused system) gives very similar results. This may explain the lack of significantly different IPS behaviour for single-source events.

Event-shapes on the other hand continue to evolve towards more compact forms with increasing  $\theta_{flow}$  (Fig.10(d),  $\Omega > 0.6$ ) as in Fig.9(b), but here we can see that, as for IPS, distributions about the mean values are comparatively wide. It should be noted that although here we mix events with different fragment multiplicities, the mean  $Z \geq 5$  multiplicity is the same for all  $\Omega > 0.4$  (Fig.10(b)) and so the evolution of the GSV truly reflects a change in event shapes, i.e. the evolution of the fragment kinematics with increasing  $\theta_{flow}$ . This evolution is complete for  $\theta_{flow} \gtrsim 70^\circ$  ( $\Omega \gtrsim 0.85$ ): it is for this reason that we choose to define our sample of single-source events (Zone 4 of Fig.7) as having  $\theta_{flow} \geq 70^\circ$  even though the distribution of relative angles between fragments for events with  $60^\circ \leq \theta_{flow} \leq 70^\circ$  is identical to that for  $\theta_{flow} \geq 70^\circ$  (see Fig.9(g)).

### 5.1 Selecting the most central collisions

Let us try to define IPS cuts corresponding to very central collisions in order to isolate single-source events. In Fig.11 the IPS-variable distributions for Zone 4 events (shaded histograms) are compared to those for all recorded events (including  ${}^{155}\text{Gd} + {}^{12}\text{C}$  collisions, lines) and for the most dissipative events (Zones 2 to 4 of Fig.7, hatched histograms). All of these variables increase monotonously with decreasing impact parameter, i.e the largest values correspond to the most central collisions (see Sec.3.2). Fig.11 shows that Zone 4 events correspond to central collisions (large IPS values) but even though they have mean values of IPS which are higher than for Zones 2 and 3 (Fig.10(b,c)), the distribution is so wide that the same values are explored by Zone 4 events as by all of the most dissipative events. This observation can be interpreted in terms of a large overlap of impact parameters leading to single-source or to ‘binary’ exit channels, with single-source events merely a subset of the most

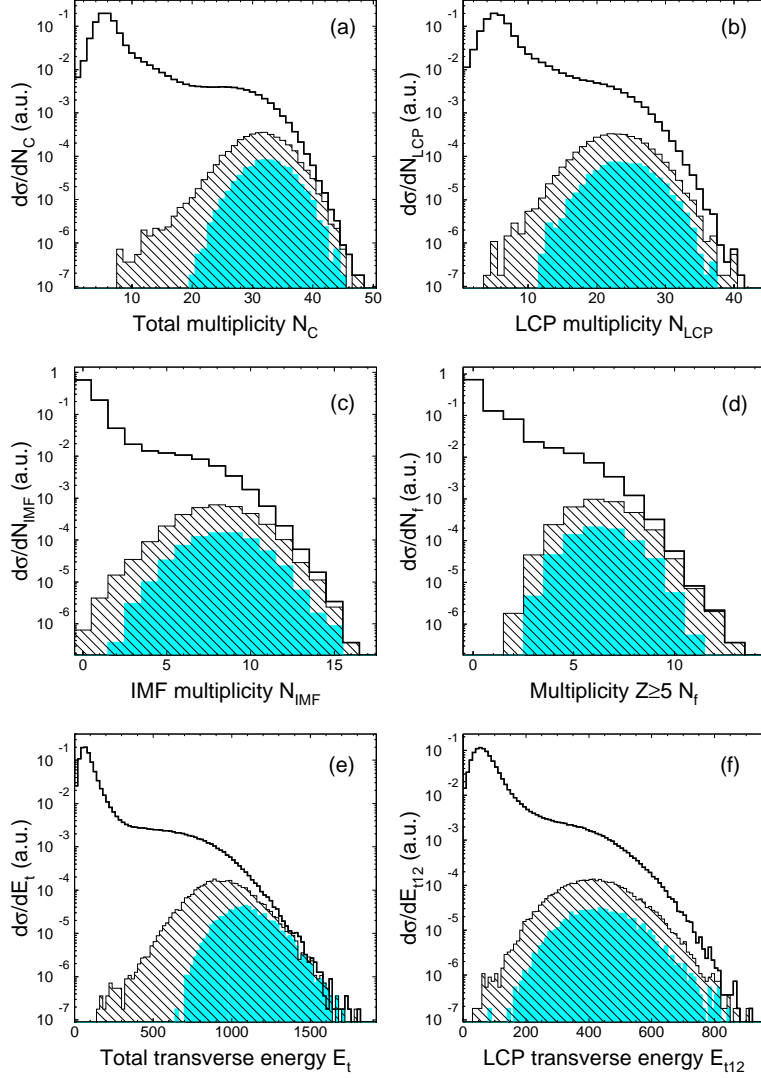


Fig. 11. Comparison of IPS distributions for all recorded events (histogram), the most dissipative events (Zones 2–4 of Fig.7, hatched histogram) and Zone 4 events (shaded histogram). All histograms are normalised with respect to the total number of recorded events.

central collisions. It is clear that no cut on an IPS variable can be defined which would isolate some or all of Zone 4 events without mixing them with the other Zones. The only exception is  $E_t$  (Fig.11(e)) for which, because large  $\theta_{\text{flow}}$  angles imply large fragment transverse energies, Zone 4 events are the only ones to explore the largest  $E_t$  values.

One may then wonder if high-multiplicity or high transverse energy cuts can be used in order to isolate a sample of single-source events different to that constituted by Zone 4 of the ‘Wilczyński diagram’. Such cuts have been applied to the most dissipative events i.e. Zones 2 to 4 of Fig.7 (we have shown that IPS are capable of distinguishing between these events and those of Zone 1,

Fig.6(a)) and the results are presented in Fig.12. The cuts are :  $N_C \geq 37$ ,  $N_{LCP} \geq 29$ ,  $E_t > 1070\text{MeV}$ ,  $E_{t12} \geq 570\text{MeV}$ . These values are slightly higher than the mean values observed for Zone 4 events (cf. Fig.11), and they were chosen in part so that the number of events retained by each cut was the same within 10%.

Flow angle distributions for the events selected with  $N_C$ ,  $N_{LCP}$  and  $E_{t12}$  cuts (Fig.12(a),(d),(j), shaded histograms) are forward-peaked and appear to be of the same form as the total distribution (thick lines) except that the proportion of events with the smallest  $\theta_{\text{flow}}$  is slightly reduced. We see that only  $\sim 10\%$  of the Zone 4 event sample is retained by these IPS cuts. It should be noted that for  $^{197}\text{Au}+^{197}\text{Au}$  35 A.MeV reactions (very similar in both total mass and available energy to the studied reactions), a much smaller total multiplicity cut ( $N_C > 24$ ) was found to be sufficient in order to isolate a sample of highly spherical events with an isotropic flow angle distribution corresponding to 10% of the total measured reaction cross-section [24]. Our results show that such a cut is completely insufficient for reactions of an otherwise identical asymmetric reaction. The cut applied to total transverse energies (Fig.12(g)) on the other hand greatly reduces the proportion of events with  $\cos \theta_{\text{flow}} > 0.5$  and the resulting  $\theta_{\text{flow}}$  distribution is nearly isotropic. The proportion of Zone 4 events retained by this cut is larger ( $\sim 30\%$ ) than for the other IPS as is to be expected from comparison of Fig.11(e) with Fig.11(a)–(d) and (f).

If any of these cuts isolates a sample of single-source events, the characteristics of the events should be independent of the flow angle. Therefore we separate the events selected with each IPS cut into two lots, those with small flow angles ( $\theta_{\text{flow}} < 70^\circ$ ) and those with large flow angles ( $\theta_{\text{flow}} \geq 70^\circ$ ). It should be recalled that the second lot is a subset of the Zone 4 event sample.

Distributions of relative angles between fragments are shown in Figs.12(b), (e), (h) and (k). In each case, the distribution has been divided by that of the Zone 4 events (Fig.9(c)), in order to highlight any differences between the two event samples (a value of 1 for all angles means that the considered distribution is identical to that for Zone 4 events). For the multiplicity and LCP total transverse energy cuts we see that in the sub-sample of events with  $\theta_{\text{flow}} < 70^\circ$ , large and small fragment-fragment angles are favoured compared to Zone 4 events (thick lines) suggesting fragment emission from two sources. This means that the  $\theta_{\text{flow}}$  distributions for events selected by these cuts are forward-peaked because they mix single-source and ‘binary’ events. On the other hand the events selected by the  $E_t$ -cut show fragment-fragment relative angle distributions which are identical to Zone 4 events independently of the subsequent division according to flow angle.

The average charge density of fragments in the different sets of events are presented as a function of their velocity along the principal axis in Figs.12(c),

$^{155}\text{Gd} + ^{\text{nat}}\text{U}$  36 A.MeV IPS cuts on most dissipative events

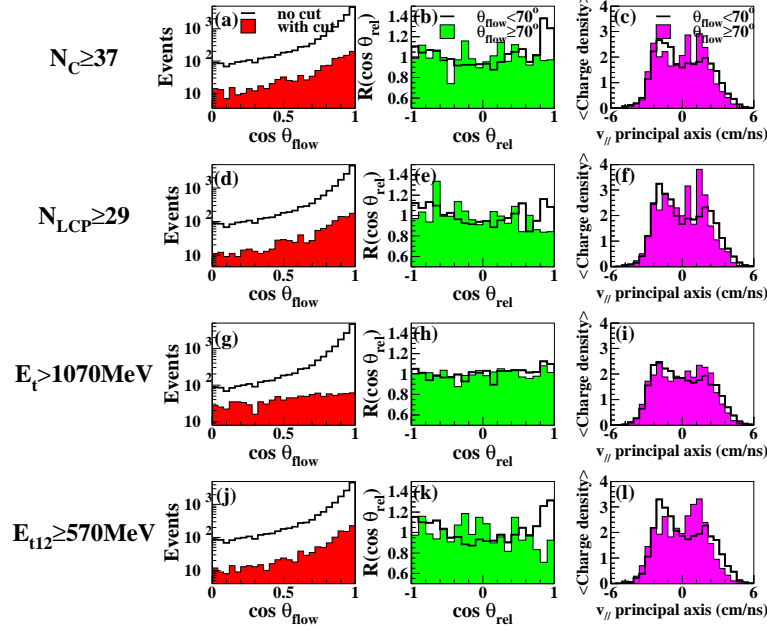


Fig. 12. Results of applying IPS cuts defined in the text to the most dissipative collisions (Zones 2–4 of Fig.7). (a),(d),(g),(j): flow angle distribution of the events selected by the IPS cut (shaded histograms) compared to the total distribution for Zones 2–4 (thick lines). (b),(e),(h),(k): distribution of fragment-fragment relative angles for IPS-selected events divided bin-by-bin by the distribution obtained for Zone 4 events (Fig.9(c)) i.e.  $R(\cos \theta_{rel}) = 1$  for identical distributions. (c),(f),(i),(l): fragment charge-velocity correlations for IPS-selected events with respect to the principal axis of each event. In the latter two cases, the events selected by IPS cut are also separated into those with  $\theta_{flow} < 70^\circ$  (thick lines) and those with  $\theta_{flow} \geq 70^\circ$  (shaded histograms).

(f), (i) and (l). The  $\theta_{flow} < 70^\circ$  subset of the events selected by cuts on  $N_C$ ,  $N_{LCP}$  and  $E_{t12}$  shows a memory of the entrance channel through the presence of larger fragments at velocities  $v_{||} < 0$ . Note also that these cuts seem to favour, among the events with  $\theta_{flow} \geq 70^\circ$ , events having a larger mean charge density for  $v_{||} > 0$  (heavier fragments emitted in the forward direction). The  $E_t$ -selected events present very homogeneous, symmetric and  $\theta_{flow}$ -independent charge-velocity correlations, although a slight increase of the mean charge density is perhaps visible at backwards velocities for  $\theta_{flow} < 70^\circ$  (Fig.12(i), thick line).

To sum up this section on the selection of the most central collisions, we have shown that the sample of single-source events found in Zone 4 of the ‘Wilczyński diagram’ is a subset of the most dissipative events as far as IPS are concerned, and are therefore probably a subset of the most central collisions. Attempts to isolate single-source events with an IPS cut supposed to select the most central collisions only result in mixed samples containing single-

source and ‘binary’ events. The exception to this rule is the total transverse energy which selects a sample of single-source events with an almost isotropic flow angle distribution, albeit with some pollution by ‘binary’ events being in evidence for the smallest  $\theta_{\text{flow}}$ .

## 5.2 Selecting the most compact event shapes

Let us now consider the selection of the most spherical (or compact) event shapes, by defining cuts using global shape variables. Fig.13 compares the event shapes of Zone 4 events with those of all the most dissipative events. For all GSV (except  $E_{\text{iso}}$  calculated with respect to the beam axis) most of the values populated by all of the most dissipative events can also be associated with Zone 4 events. In all cases it can be seen that the Zone 4 single-source event sample explores a very wide range of event shapes. One may then worry that cuts made to restrict to only the most compact event shapes will select a very particular subset of single source events (see below). As in the IPS case, it is clear that no cut on a GSV variable can be defined which would isolate all or some of the Zone 4 events without mixing them with the other Zones, except for the two ‘ambiguous’ isotropy ratios. For these GSV Zone 4 events are the only ones to explore values signifying a large proportion of fragment emission in directions perpendicular to the beam (see Sec3.3, Fig.6(d)), because these events have the largest  $\theta_{\text{flow}}$  angles.

We have defined GSV cuts supposed to select the most spherical event shapes, and in each case the size of the event sample was the same (within 10% ) as those previously selected with IPS cuts. The cuts were:  $H_2 < 0.06$ ,  $E_{\text{iso}} < 0.21$  and  $R_{\text{iso}} > 0.74$  for the ‘unambiguous’ shape variables,  $|E_{\text{iso}}| < 0.5$  and  $0.93 < R_{\text{iso}} < 1.07$  for the isotropy ratios calculated with respect to the beam axis. First, let us consider the results for the 3 ‘unambiguous’ GSV (Fig.14).

Selecting the most compact event shapes does not change greatly the form of the flow angle distributions (Fig.14(a), (d), (g)). Events with small  $\theta_{\text{flow}}$  are still favoured in the selected event samples, although the  $E_{\text{iso}}$  cut does slightly flatten the  $\cos \theta_{\text{flow}}$  distribution. The fragment-fragment relative angle distributions, on the other hand, are independent of  $\theta_{\text{flow}}$  for each GSV cut (Fig.14(b), (e), (h)). Moreover the suppression of small and large  $\theta_{\text{rel}}$  relative to the distribution for Zone 4 events is the opposite of what one would expect for samples mixing single-source and ‘binary’ events. In fact, these distributions are directly related to the GSV cuts as can be readily seen by inspection of the  $H_2$  definition, Eq.8. As  $H_2$  depends on  $\cos^2 \theta_{\text{rel}}$ , imposing small values of  $H_2$  favours events where the majority of fragment pairs have  $|\cos \theta_{\text{rel}}| \approx 0$ . Although the link between  $\theta_{\text{rel}}$  and the isotropy ratios is not so trivial to demonstrate analytically, it is very probable that the same kind of effect is in

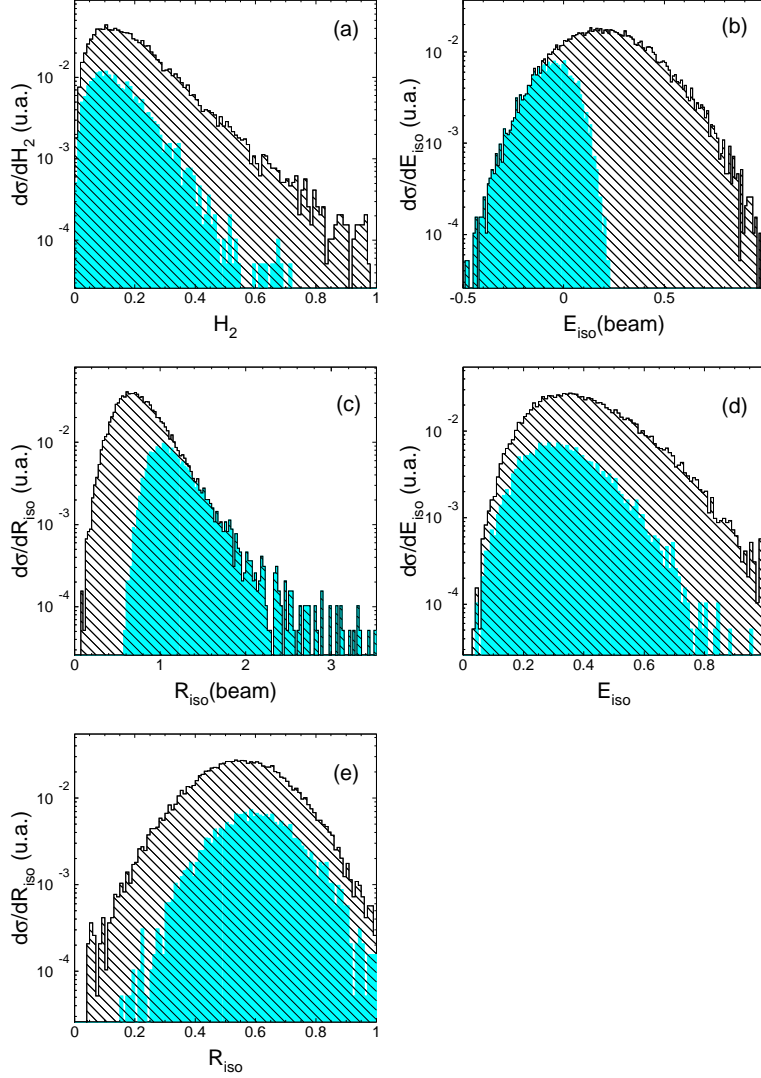


Fig. 13. Comparison of GSV distributions for the most dissipative events (hatched histogram) and single-source events ( $\theta_{\text{flow}} \geq 70^\circ$ , shaded histogram).  $E_{\text{iso}}(\text{beam})$  and  $R_{\text{iso}}(\text{beam})$  are the values calculated with respect to the beam axis (cf.  $E_{\text{iso}}^b$  and  $R_{\text{iso}}^b$  of Fig.5),  $E_{\text{iso}}$  and  $R_{\text{iso}}$  are calculated with respect to the event principal axis (cf.  $E_{\text{iso}}^{\text{P.A.}}$  and  $R_{\text{iso}}^{\text{P.A.}}$  of Fig.5). All histograms are normalised with respect to the total number of complete events.

operation also.

This is not the only non-trivial effect that cuts on ‘unambiguous’ shape variables can have on the event topology. The charge-velocity correlations show that the  $R_{\text{iso}}$  and (to a lesser degree)  $H_2$  cuts favour events in which the heaviest fragments have small velocities parallel to the principal axis. This may be a way of ‘compacting’ the event in momentum space. The charge-velocity correlations for  $E_{\text{iso}}$ -selected events on the other hand are very homogeneous, as one would naïvely expect for highly compact event shapes.

$^{155}\text{Gd} + ^{\text{nat}}\text{U}$  36 A.MeV GSV cuts on most dissipative events

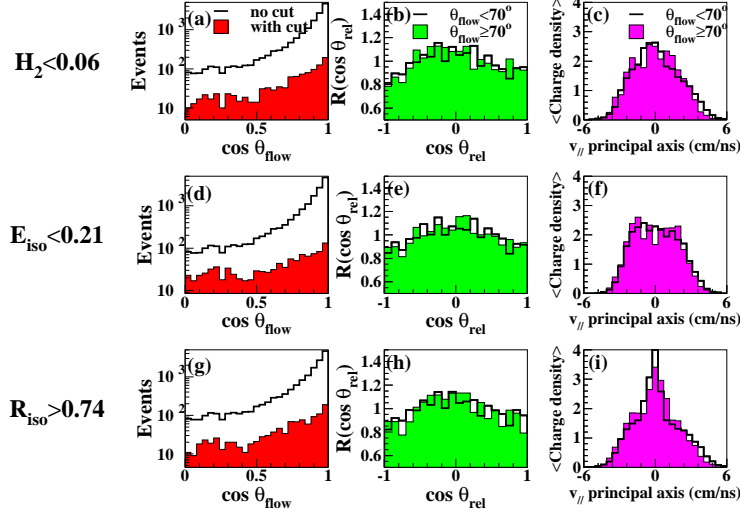


Fig. 14. Results of applying GSV cuts defined in the text to the most dissipative collisions (Zones 2–4 of Fig.7). (a),(d),(g),(j): flow angle distribution of the events selected by the GSV cut (shaded histograms) compared to the total distribution for Zones 2–4 (thick lines). (b),(e),(h),(k): distribution of fragment-fragment relative angles for GSV-selected events divided bin-by-bin by the distribution obtained for Zone 4 events (Fig.9(c)) i.e.  $R(\cos\theta_{rel}) = 1$  for identical distributions. (c),(f),(i),(l): fragment charge-velocity correlations for GSV-selected events with respect to the principal axis of each event. In the latter two cases, the events selected by GSV cut are also separated into those with  $\theta_{flow} < 70^\circ$  (thick lines) and those with  $\theta_{flow} \geq 70^\circ$  (shaded histograms).

Finally let us see what is the effect of applying to the most dissipative collisions cuts designed to select the most compact events using the two ‘ambiguous’ isotropy ratios,  $E_{iso}$  and  $R_{iso}$  calculated with respect to the beam axis. The resulting event samples do indeed appear to be good samples of single-source events: they have fragment-fragment relative angle distributions which are identical to that of Zone 4 events whatever value takes  $\theta_{flow}$  (Fig.15(b),(e)) and charge-velocity correlations show an homogeneous, symmetric distribution of the fragments in velocity space (Fig.15(c),(f)). These cuts therefore avoid the peculiar effects on event topology that are seen with the ‘unambiguous’ GSV. However Fig.15(a),(d) shows that the flow angle distribution of the selected events is unphysical, having been distorted by the correlation between the ‘ambiguous’ isotropy ratios and  $\theta_{flow}$ . Small  $\theta_{flow}$  events are strongly suppressed or even excluded (in the case of  $E_{iso}$ ) by the ‘ambiguous’ GSV cuts.

To summarise this section on selecting the most compact events, we have shown that the single-source event sample isolated in Zone 4 of the ‘Wilczyński diagram’ explores a very wide range of event shapes, therefore GSV cuts can only select subsets of single-source events with very particular fragment emission topologies. Specifically, the ‘unambiguous’ GSV select events with

$^{155}\text{Gd} + ^{\text{nat}}\text{U}$  36 A.MeV GSV cuts on most dissipative events

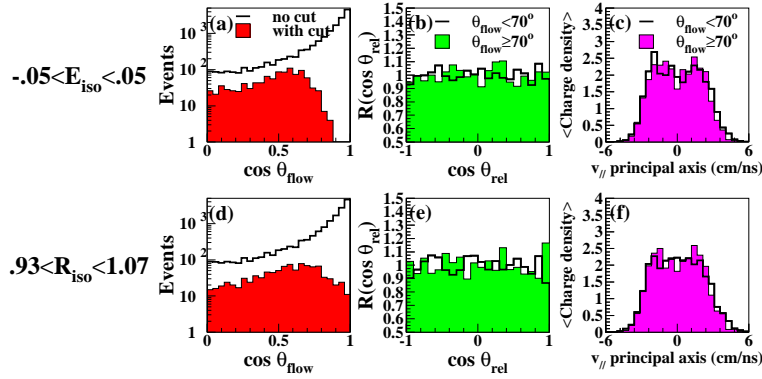


Fig. 15. Results of applying ‘ambiguous’ GSV cuts defined in the text to the most dissipative collisions (Zones 2–4 of Fig.7). (a),(d): flow angle distribution of the events selected by the GSV cut (shaded histograms) compared to the total distribution for Zones 2–4 (thick lines). (b),(e): distribution of fragment-fragment relative angles for GSV-selected events divided bin-by-bin by the distribution obtained for single-source events (Fig.9(c)) i.e.  $R(\cos \theta_{rel}) = 1$  for identical distributions. (c),(f): fragment charge-velocity correlations for GSV-selected events with respect to the principal axis of each event. In the latter two cases, the events selected by GSV cut are also separated into those with  $\theta_{flow} < 70^\circ$  (thick lines) and those with  $\theta_{flow} \geq 70^\circ$  (shaded histograms)

forward-peaked flow angle distributions, in which pairs of fragments are preferentially detected at  $90^\circ$  and the heaviest fragments are at rest in the centre of mass frame. On the other hand the isotropy ratios when calculated with respect to the beam axis permit the extraction of small- $\theta_{flow}$  single-source events which are similar to the Zone 4 event sample. However most of the single-source events with small  $\theta_{flow}$  ( $\cos \theta_{flow} < 0.3$ ) remain irrecoverable due to the strong correlation between  $\theta_{flow}$  and these variables.

## 6 Conclusions

We have shown for  $^{155}\text{Gd} + ^{\text{nat}}\text{U}$  36 A.MeV reactions measured with the INDRA  $4\pi$  detector array how a sample of single-source events may be isolated which correspond to the formation and multifragmentation of very heavy fused systems, comprising the majority of the entrance channel nucleons. These events are selected from among the most well-characterised reactions (at least 80% of the total charge and momentum were measured) using a condition on the flow angle  $\theta_{flow}$  between the principal axis of the event ellipsoid, constructed from fragment ( $Z \geq 5$ ) kinetic energies, and the beam direction. One expects events with large  $\theta_{flow}$  to show little memory of the colliding nuclei because of the forward-focused differential cross-section for deeply inelastic collisions of heavy nuclei. We have shown that a class of events compatible



with the fast break-up of a compact single source is dominant at large flow angles,  $\theta_{\text{flow}} \geq 70^\circ$ .

This sample of single-source events is associated with the largest mean multiplicities and total transverse energies of charged reaction products, and on average the most compact event shapes. However the single-source events are only a subset of the most central/most compact events, therefore isolating a sample of them using impact parameter selectors (IPS) or global shape variables (GSV) is not as trivial as it may first appear. We found that the only variables capable of isolating an event sample with the same characteristics as events with  $\theta_{\text{flow}} \geq 70^\circ$ , namely  $E_t$  the total transverse energy of charged reaction products,  $R_{\text{iso}}$  and  $E_{\text{iso}}$  the isotropy ratios of momentum and kinetic energy flow, respectively, calculated with respect to the beam axis, are all correlated with the transverse kinetic energy of the detected fragments, and this is also true for  $\theta_{\text{flow}}$ . Therefore using the present methods it is not possible to obtain an unbiased  $\theta_{\text{flow}}$  distribution (which could give important information on the relaxation in form of the multifragmenting sources, angular momentum, etc. [53,54]) for the totality of the single-source events in the data sample.

The  $\theta_{\text{flow}} \geq 70^\circ$  cut permits the study of a sample of very heavy multifragmenting systems, for which bulk properties may play a decisive role. This work is presented in the accompanying paper [31].

## References

- [1] H.R. Jaqaman, A.Z. Mekjian and L. Zamick *Phys. Rev.* **C29**(1982)2067
- [2] L. Moretto and G. Wozniak, *Ann. Rev. Nuc. & Part. Sci.* **43**(1993)379
- [3] D. Guerreau, *Nucl. Phys.* **A574**(1994)111c–130c
- [4] B. Borderie, M. Montoya, M.F. Rivet, D. Jouan, C. Cabot, H. Fuchs, D. Gardes, H. Gauvin, D. Jacquet, F. Monnet, *Phys. Lett.* **B205**(1988)26
- [5] B. Lott, S.P. Baldwin, B.M. Szabo, B.M. Quedneau, W.U. Schröder, J. Töke, L.G. Sobotka, J. Barreto, R.J. Charity, L. Gallamore, D.G. Sarantites, D.W. Stracener and R.T. De Souza, *Phys. Rev. Lett.* **68**(1992)3141
- [6] J.F. Lecolley, L. Stugge, M. Aboufirassi, A. Badala, B. Bilwes, R. Bougault, R. Brou, F. Cosmo, J. Colin, D. Durand, J. Galin, A. Genoux-Lubain, D. Guerreau, D. Horn, D. Jacquet, J.L. Laville, F. Lefebvres, C. Le Brun, J. Lemiere, O. Lopez, M. Louvel, M. Mahi, M. Morjean, C. Paulot, A. Peghaire, N. Prot, G. Rudolf, F. Scheibling, J.C. Steckmeyer, B. Tamain, S. Tomasevic, *Phys. Lett.* **B325**(1994)317
- [7] R. Bougault, J.F. Lecolley, M. Aboufirassi, A. Badala, B. Bilwes, R. Brou, J. Colin, F. Cosmo, D. Durand, J. Galin, A. Genoux-Lubain, D. Guerreau, D.

- Horn, D. Jacquet, J.L. Laville, C. Le Brun, F. Lefebvres, O. Lopez, M. Louvel, M. Mahi, M. Morjean, C. Paulot, A. Peghaire, G. Rudolf, F. Scheibling, J.C. Steckmeyer, L. Stuttgé, S. Tomasevic, B. Tamain, *Nucl. Phys.* **A587**(1995)499
- [8] J. Péter, S.C. Jeong, J.C. Angelique, G. Auger, G. Bizard, R. Brou, A. Buta, C. Cabot, Y. Cassagnou, E. Crema, D. Cussol, D. Durand, Y. El Masri, P. Eudes, Y.Z. He, A. Kerambrun, C. Lebrun, R. Legrain, J.P. Patry, A. Peghaire, R. Regimbart, E. Rosato, F. Saint-Laurent, J.C. Steckmeyer, B. Tamain, E. Vient, *Nucl. Phys.* **A593**(1995)95
- [9] V. Métivier, B. Tamain, G. Auger, Ch.O. Bacri, J. Benlliure, F. Bocage, B. Borderie, R. Bougault, R. Brou, Ph. Buchet, J.L. Charvet, A. Chbihi, J. Colin, D. Cussol, R. Dayras, A. Demeyer, D. Doré, D. Durand, P. Ecomard, Ph. Eudes, D. Gourio, D. Guinet, R. Laforest, Ph. Lantesse, J.L. Laville, L. Lebreton, J.F. Lecomte, A. Le Fèvre, R. Legrain, O. Lopez, M. Louvel, N. Marie, L. Nalpas, M. Parlog, J. Péter, E. Plagnol, A. Rahmani, T. Reposeur, M.F. Rivet, E. Rosato, F. Saint-Laurent, J.C. Steckmeyer, L. Tassan-Got, E. Vient, C. Volant, J.P. Wieleczko, *Nucl. Phys.* **A672**(2000)357
- [10] M. Lefort and Ch. Ngô, *Ann. Phys.* **3**(1978)5
- [11] W.U. Schröder and J.R. Huizenga in *Treatise on Heavy-Ion Science* Volume 2, p.115, Ed. D. Allan Bromley, Plenum Press, New York (1984)
- [12] L. Stuttgé, J.C. Adloff, B. Bilwes, R. Bilwes, F. Cosmo, M. Glaser, G. Rudolf, F. Scheibling, R. Bougault, J. Colin, F. Delaunay, A. Genoux-Lubain, D. Horn, C. Le Brun, J.F. Lecomte, M. Louvel, J.C. Steckmeyer, J.L. Ferrero, *Nucl. Phys.* **A539**(1992)511
- [13] J. Lukasik, J. Benlliure, V. Mtivier, E. Plagnol, B. Tamain, M. Assenard, G. Auger, Ch.O. Bacri, E. Bisquer, B. Borderie, R. Bougault, R. Brou, Ph. Buchet, J. L. Charvet, A. Chbihi, J. Colin, D. Cussol, R. Dayras, A. Demeyer, D. Doré, D. Durand, E. Gerlic, M. Germain, D. Gourio, D. Guinet, P. Lantesse, J.L. Laville, J.F. Lecomte, A. Le Fèvre, T. Lefort, R. Legrain, O. Lopez, M. Louvel, N. Marie, L. Nalpas, M. Parlog, J. Péter, O. Politi, A. Rahmani, T. Reposeur, M.F. Rivet, E. Rosato, F. Saint-Laurent, M. Squalli, J.C. Steckmeyer, M. Stern, L. Tassan-Got, E. Vient, C. Volant, J. P. Wieleczko, M. Colonna, F. Haddad, Ph. Eudes, T. Sami, and F. Sebille, *Phys. Rev.* **C55**(1997)1906; E. Plagnol, J. Lukasik, G. Auger, Ch. O. Bacri, N. Bellaize, F. Bocage, B. Borderie, R. Bougault, R. Brou, P. Buchet, J.L. Charvet, A. Chbihi, J. Colin, D. Cussol, R. Dayras, A. Demeyer, D. Doré, D. Durand, J.D. Frankland, E. Galichet, E. Genouin-Duhamel, E. Gerlic, D. Guinet, P. Lantesse, J.L. Laville, J.F. Lecomte, R. Legrain, N. Le Neindre, O. Lopez, M. Louvel, A.M. Maskay, L. Nalpas, A.D. Nguyen, M. Pârlog, J. Péter, M.F. Rivet, E. Rosato, F. Saint-Laurent, S. Salou, J. C. Steckmeyer, M. Stern, G. Tabacaru, B. Tamain, L. Tassan-Got, O. Tirel, E. Vient, C. Volant, and J. P. Wieleczko, *Phys. Rev.* **C61**(1999)014606
- [14] T. Lefort, D. Doré, D. Cussol, Y.G. Ma, J. Péter, R. Dayras, M. Assenard, G. Auger, Ch.O. Bacri, F. Bocage, R. Bougault, R. Brou, P. Buchet, J.L. Charvet, A. Chbihi, J. Colin, A. Demeyer, D. Durand, P. Eudes, J.D. Frankland, E.

- Galichet, E. Genouin-Duhamel, E. Gerlic, M. Germain, D. Gourio, D. Guinet, B. Hurst, P. Lautesse, J.L. Laville, J.F. Lecomte, A. Le Fevre, R. Legrain, N. Le Neindre, O. Lopez, M. Louvel, A.M. Maskay, L. Nalpas, A.D. N'Guyen, M. Parlog, E. Plagnol, G. Politi, A. Rahmani, T. Reposeur, E. Rosato, F. Saint-Laurent, S. Salou, J.C. Steckmeyer, M. Stern, G. Tabacaru, B. Tamain, L. Tassan-Got, O. Tirel, E. Vient, C. Volant, J.P. Wieleczko, A. Wieloch, *Nucl. Phys.* **A662**(2000)397–422
- [15] Ph. Eudes, Z. Basrak, F. Sébille, *Phys. Rev.* **C56**(1997)2003
- [16] P. Pawlowski, B. Borderie, G. Auger, Ch.O. Bacri, N. Bellaize, F. Bocage, R. Bougault, R. Brou, Ph. Buchet, J.L. Charvet, A. Chbihi, J. Colin, D. Cussol, R. Dayras, A. Demeyer, D. Doré, D. Durand, J.D. Frankland, E. Galichet, E. Genouin-Duhamel, E. Gerlic, D. Guinet, Ph. Lautesse, J.L. Laville, J.F. Lecomte, R. Legrain, N. Le Neindre, O. Lopez, M. Louvel, A.M. Maskay, L. Nalpas, A.D. Nguyen, M. Parlog, J. Péter, E. Plagnol, M.F. Rivet, E. Rosato, F. Saint-Laurent, S. Salou, J.C. Steckmeyer, M. Stern, G. Tabacaru, B. Tamain, L. Tassan-Got, O. Tirel, E. Vient, C. Volant, J.P. Wieleczko, submitted to *Phys. Rev. C*
- [17] A.A. Stefanini, G. Casini, P.R. Maurenzig, A. Olmi, R.J. Charity, R. Freifelder, A. Gobbi, N. Herrmann, K.D. Hildenbrand, M. Petrovici, F. Rami, H. Stelzer, J.P. Wessels, M. Gnirs, D. Pelte, J. Galin, D. Guerreau, U. Jahnke, A. Péghaire, J.C. Adloff, B. Bilwes, R. Bilwes and G. Rudolf, *Z. Phys.* **A351**(1995)167
- [18] F. Bocage, J. Colin, M. Louvel, G. Auger, Ch.O. Bacri, N. Bellaize, B. Borderie, R. Bougault, R. Brou, P. Buchet, J.L. Charvet, A. Chbihi, D. Cussol, R. Dayras, A. Demeyer, D. Doré, D. Durand, J.D. Frankland, E. Galichet, E. Genouin-Duhamel, E. Gerlic, D. Guinet, P. Lautesse, J.L. Laville, J.F. Lecomte, R. Legrain, N. Le Neindre, O. Lopez, A.M. Maskay, L. Nalpas, A.D. Nguyen, M. Parlog, J. Péter, E. Plagnol, M.F. Rivet, E. Rosato, F. Saint-Laurent, S. Salou, J.C. Steckmeyer, M. Stern, G. Tabacaru, B. Tamain, O. Tirel, L. Tassan-Got, E. Vient, C. Volant, J.P. Wieleczko, *Nucl. Phys.* **A** in press.
- [19] C.P. Montoya, W.G. Lynch, D.R. Bowman, G.F. Peaslee, N. Carlin, R.T. de Souza, C.K. Gelbke, W.G. Gong, Y.D. Kim, M.A. Lisa, L. Phair, M.B. Tsang, J.B. Webster, C. Williams, N. Colonna, K. Hanold, M.A. McMahan, G.J. Wozniak and L.G. Moretto, *Phys. Rev. Lett.* **73**(1994)3070
- [20] J. Töke, B. Lott, S.P. Baldwin, B.M. Quedeneau, W.U. Schröder, L.G. Sobotka, J. Barreto, R.J. Charity, L. Gallamore, D.G. Sarantites, D.W. Stracener, and R.T. De Souza, *Nucl. Phys.* **A583**(1995)519
- [21] J.F. Lecomte, L. Stuttgé, M. Aboufirassi, B. Bilwes, R. Bougault, R. Brou, F. Cosmo, J. Colin, D. Durand, J. Galin, A. Genoux-Lubain, D. Guerreau, D. Horn, D. Jacquet, J.L. Laville, F. Lefebvres, C. Le Brun, O. Lopez, M. Louvel, M. Mahi, C. Meslin, M. Morjean, A. Peghaire, G. Rudolf, F. Scheibling, J.C. Steckmeyer, B. Tamain, S. Tomasevic, *Phys. Lett.* **B354**(1995)202
- [22] Y. Larochelle, L. Gingras, L. Beaulieu, X. Qian, Z. Saddiki, B. Djerroud, D. Doré, R. Laforest, R. Roy, M. Samri, C. St-Pierre, G.C. Ball, D.R. Bowman, A.

- Galindo-Uribarri, E. Hagberg, D. Horn, J.A. López, T. Robinson, *Phys. Rev.* **C55**(1997)1869
- [23] J.F. Lecomte, D. Durand, M. Aboufirassi, R. Bougault, J. Colin, A. Genoux-Lubain, C. Le Brun, O. Lopez, M. Louvel, C. Meslin, G. Rudolf, L. Stuttgé and S. Tomasevic, *Phys. Lett.* **B387**(1996)460
- [24] Multics/Miniball Collaboration: M. D'Agostino, P.F. Mastinu, P.M. Milazzo, M. Bruno, D.R. Bowman, P. Buttazzo, L. Celano, N. Colonna, J.D. Dinius, A. Ferrero, M.L. Fiandri, C.K. Gelbke, T. Glasmacher, F. Gramegna, D.O. Handzy, D. Horn, W.C. Hsi, M. Huang, I. Iori, G.J. Kunde, M.A. Lisa, W.G. Lynch, L. Manduci, G.V. Margagliotti, C.P. Montoya, A. Moroni, G.F. Peaslee, F. Petruzzelli, L. Phair, R. Rui, C. Schwarz, M.B. Tsang, G. Vannini and C. Williams, *Phys. Lett.* **B368**(1996)259
- [25] N. Marie, R. Laforest, R. Bougault, J.P. Wieleczko, D. Durand, Ch.O. Bacri, J.F. Lecomte, F. Saint-Laurent, G. Auger, J. Benlliure, E. Bisquer, B. Borderie, R. Brou, J.L. Charvet, A. Chbihi, J. Colin, D. Cussol, R. Dayras, E. De Filippo, A. Demeyer, D. Doré, P. Ecomard, P. Eudes, D. Gourio, D. Guinet, P. Lantesse, J.L. Laville, A. Le Fevre, T. Lefort, R. Legrain, O. Lopez, M. Louvel, V. Métivier, L. Nalpas, A. Ouatzerga, M. Parlog, J. Péter, E. Plagnol, A. Rahmani, T. Reposeur, M.F. Rivet, E. Rosato, S. Salou, M. Squalli, J.C. Steckmeyer, B. Tamain, L. Tassan-Got, E. Vient, C. Volant, *Phys. Lett.* **B391**(1997)15
- [26] G. Bertsch and P.J. Siemens, *Phys. Lett.* **B126**(1983)9
- [27] M. Colonna and Ph. Chomaz, *Phys. Rev.* **C49**(1994)1908; M. Colonna, Ph. Chomaz and J. Randrup, *Nucl. Phys.* **A567**(1994)637
- [28] M.F. Rivet, Ch.O. Bacri, B. Borderie, J.D. Frankland, M. Assenard, G. Auger, F. Bocage, R. Bougault, R. Brou, P. Buchet, A. Chbihi, J. Colin, R. Dayras, A. Demeyer, D. Doré, D. Durand, P. Eudes, E. Galichet, E. Genouin-Duhamel, E. Gerlic, M. Germain, D. Guinet, P. Lantesse, J.L. Laville, J.F. Lecomte, A. Le Fevre, T. Lefort, R. Legrain, N. Le Neindre, O. Lopez, M. Louvel, L. Nalpas, A.D. Nguyen, M. Parlog, J. Péter, E. Plagnol, A. Rahmani, T. Reposeur, E. Rosato, F. Saint-Laurent, S. Salou, M. Squalli, J.C. Steckmeyer, M. Stern, G. Tabacaru, B. Tamain, L. Tassan-Got, O. Tirel, D. Vintache, C. Volant, J.P. Wieleczko, A. Guarnera, M. Colonna, Ph. Chomaz, *Phys. Lett.* **B430**(1998)215
- [29] B. Borderie, B. Remaud, M.F. Rivet, F. Sebille, *Phys. Lett.* **B302**(1993)15
- [30] B. Jouault, G. Royer, F. Haddad, F. Sebille, *Nucl. Phys.* **A615**(1997)82
- [31] J.D. Frankland, B. Borderie, M. Colonna, M.F. Rivet, Ch.O. Bacri, Ph. Chomaz, D. Durand, A. Guarnera, M. Parlog, M. Squalli, G. Tabacaru, G. Auger, N. Bellaize, F. Bocage, R. Bougault, R. Brou, P. Buchet, A. Chbihi, J. Colin, D. Cussol, R. Dayras, A. Demeyer, D. Doré, E. Galichet, E. Genouin-Duhamel, E. Gerlic, D. Guinet, P. Lantesse, J.L. Laville, J.F. Lecomte, R. Legrain, N. Le Neindre, O. Lopez, M. Louvel, A.M. Maskay, L. Nalpas, A.D. Nguyen, E. Plagnol, E. Rosato, F. Saint-Laurent, S. Salou, J.C. Steckmeyer, B.

- Tamain, L. Tassan-Got, O. Tirel, E. Vient, C. Volant, J.P. Wieleczko (INDRA collaboration), accompanying paper submitted to *Nucl. Phys. A*
- [32] J. Pouthas, B. Borderie, E. Plagnol, M.F. Rivet, F. Saint-Laurent, J.C. Steckmeyer, G. Auger, Ch.O. Bacri, S. Barbey, A. Barbier, A. Benkirane, J. Benlliure, P. Bourgault, P. Box, R. Bzyl, D. Charlet, J.L. Charvet, A. Chbihi, T. Clerc, N. Copinet, D. Cussol, M. Engrand, J.M. Gautier, Y. Huguet, O. Jouniaux, J.L. Laville, P. Lelong, P. Osrin, L. Olivier, S. Pierre, B. Piquet, E. Plaige, B. Raine, A. Richard, J. Ropert, C. Spitaels, L. Stab, D. Sznajderman, L. Tassan-Got, J. Tillier, M. Tripon, P. Vallerand, P. Volkov, J.P. Wieleczko, G. Wittwer, *Nucl. Instr. and Meth. in Phys. Res.* **A357**(1995)418
- [33] J. Pouthas, A. Bertaut, B. Borderie, P. Bourgault, B. Cahan, G. Carles, D. Charlet, D. Cussol, R. Dayras, M. Engrand, O. Jouniaux, P. Le Botlan, A. Leconte, P. Lelong, L. Martina, P. Mosrin, L. Olivier, J.P. Passerieux, B. Piquet, E. Plagnol, E. Plaige, B. Raine, A. Richard, F. Saint-Laurent, C. Spitaels, J. Tillier, M. Tripon, P. Vallerand, P. Volkov and G. Wiittwer, *Nucl. Inst. and Meth. in Phys. Res.* **A369**(1996)222
- [34] G. Tabacaru, B. Borderie, A. Ouatzizerga, M. Parlog, M.F. Rivet, G. Auger, Ch.O. Bacri, F. Bocage, R. Bougault, R. Brou, Ph. Buchet, J.L. Charvet, A. Chbihi, J. Colin, D. Cussol, R. Dayras, A. Demeyer, D. Doré, D. Durand, P. Ecomard, J.D. Frankland, E. Galichet, E. Genouin-Duhamel, E. Gerlic, D. Guinet, P. Loutesse, J.L. Laville, A. Le Fevre, T. Lefort, R. Legrain, N. Le Neindre, O. Lopez, M. Louvel, L. Nalpas, A.D. Nguyen, E. Plagnol, E. Rosato, F. Saint-Laurent, S. Salou, M. Squalli, J.C. Steckmeyer, M. Stern, L. Tassan-Got, O. Tirel, E. Vient, C. Volant, J.P. Wieleczko, *Nucl. Instr. and Meth. in Phys. Res.* **A428**(1999)379–390
- [35] M. Parlog, B. Borderie, M.F. Rivet, G. Tabacaru, A. Chbihi, M. Elouardi, N. Le Neindre, O. Lopez, E. Plagnol, L. Tassan-Got, G. Auger, Ch.O. Bacri, N. Bellaize, F. Bocage, R. Bougault, B. Bouriquet, R. Brou, Ph. Buchet, J.L. Charvet, J. Colin, D. Cussol, R. Dayras, A. Demeyer, D. Doré, D. Durand, J.D. Frankland, E. Galichet, E. Genouin-Duhamel, E. Gerlic, S. Hudan, D. Guinet, Ph. Loutesse, F. Lavaud, J.L. Laville, J.F. Lecolley, C. Leduc, R. Legrain, M. Louvel, A.M. Maskay, L. Nalpas, J. Normand, J. Péter, E. Rosato, F. Saint-Laurent, J.C. Steckmeyer, B. Tamain, O. Tirel, E. Vient, C. Volant, J.P. Wieleczko, submitted to *Nucl. Instr. and Meth. in Phys. Res. A*
- [36] W.W. Wilcke et al., *At. Dat. and Nuc. Dat. Table* **25**(1980)391
- [37] C. Cavata, M. Demoulin, J. Gosset, M.C. Lemaire, D. L'Hote, J. Poitou, O. Valette, *Phys. Rev.* **C42**(1990)1760
- [38] J. Péter, D. Cussol, G. Bizard, R. Brou, M. Louvel, J.P. Patry, R. Regimbart, J.C. Steckmeyer, J.P. Sullivan, B. Tamain, E. Crema, H. Doubre, K. Hagel, G.M. Jin, A. Peghaire, F. Saint-Laurent, Y. Cassagnou, R. Legrain, C. Lebrun, E. Rosato, R. Macgrath, S.C. Jeong, S.M. Lee, Y. Nagashima, T. Nakagawa, M. Ogihara, J. Kasagi, T. Motobayashi, *Nucl. Phys.* **A519**(1990)611
- [39] J.D. Frankland, Thesis, Université de Paris-Sud Orsay, 1998 (IPNO-T-98-06)

- [40] A. Schüttauf, W.D. Kunze, A. Wörner, M. Begemann-Blaich, Th. Blaich, D.R. Bowman, R.J. Charity, A. Cosmo, A. Ferrero, C.K. Gelbke, C. Groß, W.C. Hsi, J. Hubele, G. Immé, I. Iori, J. Kempfer, P. Kreutz, G.J. Kunde, V. Lindenstruth, M.A. Lisa, W.G. Lynch, U. Lynen, M. Mang, T. Möhlenkamp, A. Moroni, W.F.J. Müller, M. Neumann, B. Ocker, C.A. Ogilvie, G.F. Peaslee, J. Pochodzalla, G. Raciti, F. Rosenberger, Th. Rubehn, H. Sann, C. Schwarz, W. Seidel, V. Serfling, L.G. Sobotka, J. Stroth, L. Stuttgé, S. Tomasevic, W. Trautmann, A. Trzcinski, M.B. Tsang, A. Tucholski, G. Verde, C.W. Williams, E. Zude and B. Zwieglinski, *Nucl. Phys.* **A607**(1996)457
- [41] W.J. Llope et al. (The NSCL  $4\pi$  Group), MSU preprint MSUCL-900 (1993)
- [42] R. Barlow, *Rep. Prog. Phys.* **56**(1993)1102–1122
- [43] J. Cugnon and D. L'Hote, *Nucl. Phys.* **A397**(1983)519
- [44] G.C. Fox and S. Wolfram, *Phys. Lett.* **B82**(1979)134
- [45] A. Kerambrun, Thesis, Université de Caen, 1993 (LPCC T 93-02)
- [46] B. Tamain and D. Durand, Multifragmentation of Nuclei, in: H. Nifenecker, J.-P. Blaizot, G.F. Bertsch, W. Weise and F. David eds., *UJFG LES HOUCHEs Session LXVI, Trends in Nuclear Physics 100 Years Later* (Elsevier, 1998) p.295
- [47] H.G. Ritter, *Nucl. Phys.* **A488**(1988)651c
- [48] P. Danielewicz and M. Gyulassy, *Phys. Lett.* **B129**(1983)283
- [49] J. Wilczyński, *Phys. Lett.* **B47**(1973)484
- [50] J.F. Lecomte, E. Galichet, D. Guinet, R. Bougault, F. Gulminelli, G. Auger, Ch.O. Bacri, F. Bocage, B. Borderie, R. Brou, P. Buchet, J.L. Charvet, A. Chbihi, J. Colin, D. Cussol, R. Dayras, A. Demeyer, D. Doré, D. Durand, J.D. Frankland, E. Genouin-Duhamel, E. Gerlic, P. Lantesse, J.L. Laville, T. Lefort, R. Legrain, N. Le Neindre, O. Lopez, M. Louvel, A.M. Maskay, L. Nalpas, A.D. Nguyen, M. Parlog, J. Péter, E. Plagnol, M.F. Rivet, F. Saint-Laurent, S. Salou, J.C. Steckmeyer, M. Stern, G. Tabacaru, B. Tamain, L. Tassan-Got, O. Tirel, E. Vient, C. Volant, J.P. Wieleczko, *Nucl. Instr. and Meth. in Phys. Res.* **A441**(2000)517–524
- [51] H. Fuchs and K. Möring, *Rep. Prog. Phys.* **57**(1994)231
- [52] A.M. Maskay, Thesis, Université de Lyon 1999 (LYCEN-T 9969) and P. Desesquelles, A.M. Maskay, Ph. Lantesse, A. Demeyer, E. Gerlic, D. Guinet, M. Stern, J.L. Laville, G. Auger, Ch.O. Bacri, N. Bellaize, F. Bocage, B. Borderie, R. Bougault, B. Bouriquet, R. Brou, Ph. Buchet, D. Durand, J.D. Frankland, E. Genouin-Duhamel, S. Hudan, F. Lavaud, J.F. Lecomte, C. Leduc, R. Legrain, N. Le Neindre, O. Lopez, M. Louvel, L. Nalpas, J. Normand, M. Parlog, M.F. Rivet, E. Rosato, F. Saint-Laurent, J.C. Steckmeyer, G. Tabacaru, B. Tamain, L. Tassan-Got, O. Tirel, E. Vient, M. Vigilante, C. Volant, J.P. Wieleczko (INDRA collaboration), to be published in *Phys. Rev.* **C**

- [53] A. Le Fèvre, M. Ploszajczak and V.D. Toneev, *Phys. Rev.* **C60**(1999)051602(R)
- [54] B. Bouriquet, J.P. Wieleczko et al. (INDRA collaboration), in preparation.
- [55] J. Töke, D.K. Agnihotri, S.P. Baldwin, B. Djerroud, B. Lott, B.M. Quednau, W. Skulski, W.U. Schröder, L.G. Sobotka, R.J. Charity, D.G. Sarantites and R.T. de Souza, *Phys. Rev. Lett.* **77**(1996)3514
- [56] V.E. Viola, *Phys. Rev.* **C31**(1985)1550
- [57] M. Brack, C. Guet, H.B. Hakanson, *Phys. Rep.* **123**(1985)275